AGU PUBLICATIONS

Tectonics

RESEARCH ARTICLE
10.1002/2016TC004407

Key Points:
- Zoned hydrothermal monazite dated through SIMS U-Th-Pb isotope measurements
- Dating of multiple low-temperature deformation events in a shear zone
- Coeval deformation in the central Aar Massif and along the Rhone-Simplon Line

Supporting Information:
- Table S1
- Table S2
- Figure S1

Correspondence to:
C. Bergemann,
christian.bergemann@unige.ch

Citation:
Bergemann, C., E. Gnos, A. Berger, M. Whitehouse, J. Mullis, P. Wehrens, T. Pettke, and E. Janots (2017), Th-Pb ion probe dating of zoned hydrothermal monazite and its implications for repeated shear zone activity: An example from the Central Alps, Switzerland, *Tectonics*, *36*, 671–689, doi:10.1002/2016TC004407.

Received 28 OCT 2016
Accepted 10 MAR 2017
Accepted article online 13 MAR 2017
Published online 10 APR 2017

Th-Pb ion probe dating of zoned hydrothermal monazite and its implications for repeated shear zone activity: An example from the Central Alps, Switzerland

C. Bergemann[1], E. Gnos[2], A. Berger[3], M. Whitehouse[4], J. Mullis[5], P. Wehrens[3], T. Pettke[3], and E. Janots[6]

[1]Earth and Environmental Sciences, University of Geneva, Geneva, Switzerland, [2]Natural History Museum of Geneva, Geneva, Switzerland, [3]Institut für Geologie, University of Bern, Bern, Switzerland, [4]Swedish Museum of Natural History, Stockholm, Sweden, [5]Institute of Mineralogy and Petrography, Formerly at University of Basel, Basel, Switzerland, [6]ISTerre, Grenoble, France

Abstract Th-Pb age dating of zoned hydrothermal monazite from alpine-type fissures/clefts is a powerful tool for constraining polyphase deformation at temperatures below 350°C and presents an alternative to K/Ar and $^{40}Ar/^{39}Ar$ dating techniques for dating brittle tectonics. This study considers the relationship between cleft orientations in ductile shear zones and cleft mineral crystallization during subsequent brittle overprinting. In the Grimsel area, located in the Aar Massif of the Central Alps, horizontal clefts formed during a primary thrust dominated deformation, while younger and vertically oriented clefts developed during secondary strike-slip movements. The change is due to a switch in orientation between the principal stress axes σ_2 and σ_3. The transition is associated with monazite crystallization and chloritization of biotite at around 11.5 Ma. Quartz fluid inclusion data allow a link between deformation stages and temperatures to be established and indicate that primary monazite crystallization occurred in both cleft systems at 300–350°C. While cleft monazite crystallization ceases at ~11 Ma in inactive shear zones, monazite growth, and/or dissolution-reprecipitation continues under brittle deformation conditions in vertical clefts during later deformation until ~7 Ma. This younger shear zone activity occurs in association with dextral strike-slip movement of the Rhone-Simplon fault system. With the exception of varying Th/U values correlated with the degree of oxidation, there is only limited compositional variation in the studied cleft monazites.

1. Introduction

Alpine clefts, representing fluid-filled pockets in veins, occur predominantly within or near brittle-ductile shear zones, but also other areas that experienced brittle-ductile transitional deformation at depth. In the Grimsel area of the Aar massif the clefts formed inside or near the shear zones at abrupt rheological changes, within the more rigid and therefore brittle deforming layers. Thus, mineral crystallization ages from such clefts can provide important information about the structural evolution of individual rock packages within an orogen. In addition, clefts provide information on the fluid environment. Dissolution-precipitation reactions at medium to low temperatures within the clefts have the potential to preserve the timing of successive deformation phases in stepwise grown large crystals. In combination with structural data, fluid inclusion data, and mineral zonation-structures, the dating of cleft minerals therefore allows major deformation stages to be resolved during the retrograde deformation history.

Generally, constraining formation age and duration of deformation in lower greenschist-facies shear zones is a challenging task. Synkinematically grown and datable minerals in such shear zones, most commonly micas, are $<100\,\mu m$ in size and may consist of intergrowths of relict host rock minerals with newly crystallized material [e.g., *Rolland et al*., 2009]. The $^{40}Ar/^{39}Ar$ technique is often applied to date K-bearing minerals which have the great advantage of being practically ubiquitous and can also provide additional compositional information that helps to distinguish growth generations. However, potential inheritance of daughter isotopes or loss of mother isotopes during fluid interaction can present a challenge. In this study hydrothermal cleft monazite is used as an alternative that, although being far less common (usually only very few crystals can be found in monazite bearing clefts) and more restricted in its occurence, has the advantage of recording crystallization ages and having virtually no diffusion under the prevalent *P-T* conditions.

Greenshist-facies shear zones typically develop at midcrustal level where fluid-rock interaction and fluid-assisted fracturing of the rock will occur, if sufficient fluid is available during deformation. Fissures and

open cracks, commonly oriented perpendicular to foliation and lineation, become filled with almost incompressible fluid but will close if shearing continues, causing rotation of the clefts into the plane of flattening and expulsion of the fluid. Greenschist-facies shear zones typically produce neocrystallized or recrystallized mineral grains $<100\,\mu m$ in size [e.g., *Rolland et al*., 2009], whereas minerals in clefts are usually millimeter- to centimeter-sized due to the presence of abundant fluid. Continuous, cyclic, or episodic growth or dissolution of minerals in such clefts is determined by a variety of factors. Temperature-dependent changes in fluid saturation levels, chemical disequilibrium due to deformation causing exposure of unaltered rock, and fluid transport may all play a role [e.g., *Poty*, 1969; *Mullis et al*., 1994; *Sharp et al*., 2005]. Due to chemical disequilibrium, fluid-rock interaction causes leaching and partial mineral dissolution from the wall rock, leading to porosity in the adjacent wall rock [e.g., *Mercolli et al*., 1984; *Heijboer*, 2006]. The associated potential oversaturation in the cleft can be reached by cooling, fluid pressure drop, or fluid mixing/unmixing [*Mullis*, 1976]. However, also cleft deformation, collapse of cleft wall sections, and related exposure to less strongly leached wall rock all lead to chemical disequilibrium initiating a new dissolution-precipitation cycle. For this reason cleft minerals are generally strongly zoned and in the study region contain different sets of aqueous fluid inclusions with small amounts of CO_2 [e.g., *Poty et al*., 1974; *Mullis*, 1996]. Due to the presence of fluid in the cleft reactions can take place even at temperatures below 300°C within the cleft [e.g., *Berger et al*., 2013; *Gnos et al*., 2015], in contrast to massive mineral veins and country rocks. Due to this continued reactivity, clefts contain many minerals that crystallize at temperatures at which minerals suitable for geochronology only exceptionally form in deformed country rocks. Some cleft minerals become overgrown by other minerals, protecting them from dissolution during changing chemical conditions of the cleft fluid. While the interaction of wall rock leaching and cleft mineralization shows evidence for a locally closed system [e.g., *Sharp et al*., 2005], later re-opening has also been observed at times [e.g., *Mullis*, 1976; *Mullis et al*., 1994]. Due to these processes, the mineral association found in the cleft is often different from that found in the rocks and does not represent an equilibrium paragenesis. Dateable minerals in such clefts often include biotite, white micas, and feldspars (usually albite and/or adularia), but also monazite, xenotime, apatite, and titanite (although those titanites analyzed by the authors did not contain sufficient U for dating) can occasionally be found.

Monazite (a rare earth element (REE) phosphate) is commonly used for Th-Pb or U-Pb dating in a variety of settings ranging from magmatic to metamorphic to hydrothermal conditions. This is possible due to generally low diffusion rates of Pb [e.g., *Cherniak and Pyle*, 2008; *Gardés et al*., 2006] and its apparent resilience to metamictization [e.g., *Meldrum et al*., 1998, 1999, 2000; *Nasdala et al*., 1999]. Clefts typically form below ~450°C [e.g., *Mullis et al*., 1994; *Mullis*, 1996], and cleft monazite ages therefore always represent crystallization ages and/or important dissolution-reprecipitation stages. By dating individual domains, growth durations can be deduced in some cases [e.g., *Gasquet et al*., 2010; *Janots et al*., 2012; *Berger et al*., 2013; *Gnos et al*., 2015]. This means that cleft monazite has the potential to record both deformation and exhumation events. However, due to its late crystallization in most cases it does not yield the initial time of formation of the cleft.

In the Alps major deformation phases are generally well established. In the case of the Grimsel pass study area located in the Aar Massif in the Central Alps (Figure 1) there exists a large set of studies on the different shear zones [e.g., *Jäger et al*., 1967; *Marquer et al*., 1985; *Dempster*, 1986; *Marquer*, 1989; *Michalski and Soom*, 1990; *Challandes et al*., 2008; *Rolland et al*., 2009; *Goncalves et al*., 2012; *Wehrens*, 2015]. The shear zones are particularly well exposed in glacially polished outcrops and in underground tunnels excavated for production of hydroelectricity and for the Grimsel test site (NAGRA).

In this work, cleft monazite Th-Pb secondary ion mass spectrometry (SIMS) ages are combined with structural and fluid inclusion data. The results show the power of this method for constraining the retrograde deformation history in low-grade metamorphic areas of complex tectonic history such as the Grimsel area. The aim of the study is therefore threefold: (1) to provide additional age constraints on the tectonic evolution of the Aar-Massif during its exhumation history, (2) to demonstrate that dating of cleft monazite is a powerful method to date deformation phases and shear zone evolution in low-grade metamorphic rocks, and (3) to establish a link between fluid inclusions, monazite growth, and deformation stages.

2. Geological and Tectonic Setting

The Alpine orogen is the result of the closing of the European Tethys ocean followed by collision of the Eurasian with the Apulian plate [e.g., *Schmid et al*., 2004]. Shortening during orogenesis was accomodated

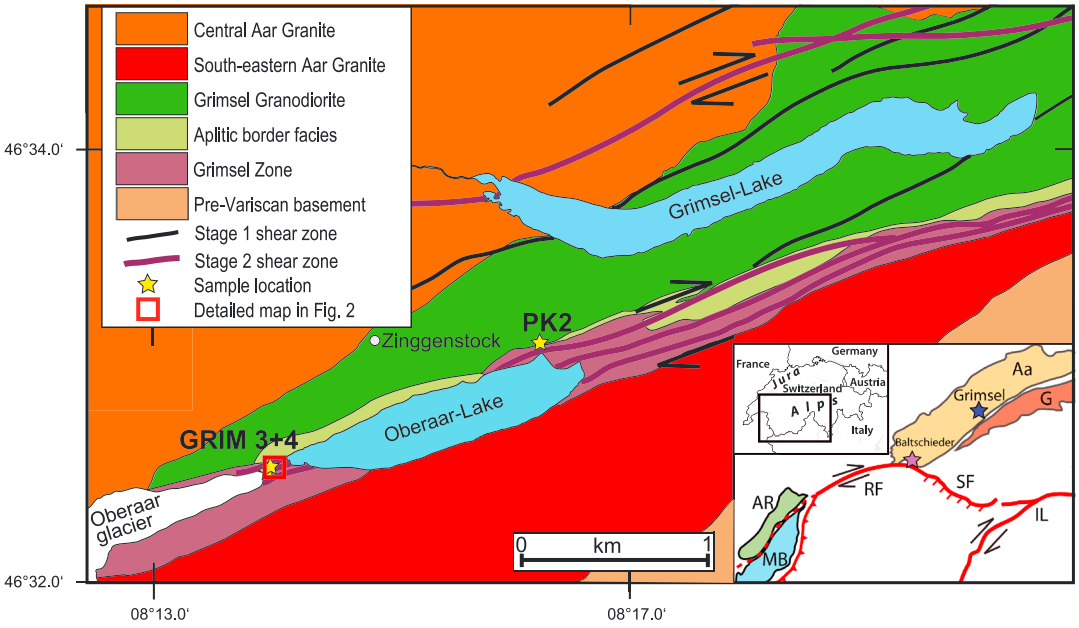

Figure 1. Geological map of the Grimsel pass region based on *Wehrens* [2015]. Inset shows tectonic sketch with the locations of Aar Massif, Baltschieder Valley, and the Rhône-Simplon fault. Aa, Aar Massif; G, Gotthard Massif; AR, Aiguilles Rouge Massif; MB, Mont Blanc Massif; RF, Rhone Fault; SF, Simplon Fault; IL, Insubric Line.

by thrusting and lateral escape of rock units locally resulting in the formation of shear zones. External massifs such as the Aar Massif in which the Grimsel area is located (Figure 1) are basement rocks of the European margin. The external massifs were strongly affected by thick-skinned thrusting during the Alpine orogeny. For the Aar Massif as a whole, up to six phases of deformation can be distinguished [*Steck*, 1968], with up to four phases of deformation recognizable in the Grimsel area [*Mullis*, 1996; *Hofmann et al*., 2004; *Challandes et al*., 2008; *Rolland et al*., 2009; *Goncalves et al*., 2012; *Rossi and Rolland*, 2014; *Wehrens*, 2015; *Diamond and Tarantola*, 2015].

Stage 1 shear zones formed during NW directed thrusting. They strike NE-SW to ENE-WSW, show steep foliation and steeply SE plunging lineation, with mainly reverse faulting shear senses [e.g., *Rolland et al*., 2009; *Wehrens*, 2015]. These shear zones contain newly formed biotite in mylonites and represent a late stage of shearing that started earlier during the main foliation observable in all parts of the Aar Massif. Fluid inclusion data give conditions of 450°C and 440 MPa [*Mullis*, 1996], but recent *P-T-t* models assumed pressure conditions of 600–650 ± 100 MPa based on phengite geobarometry [*Challandes et al*., 2008; *Goncalves et al*., 2012]. Biotite and white mica Ar-Ar ages indicate activity from ~21 Ma down to at least ~17 Ma [*Challandes et al*., 2008; *Rolland et al*., 2009]. The clefts in stage 1 shear zones have a subhorizontal orientation, perpendicular to the steeply plunging lineation (Figures 2 and 3). Clefts of this generation occur also outside of shear zones. In contrast to this, stage 2 shear zones are dominated by white mica and chlorite but formed already in the biotite stability field. They are also NE-SW and ENE-WSW oriented and subhorizontal to oblique, with slightly east plunging stretching lineations. Shear sense indicators show dextral strike-slip movement, with white mica Ar-Ar ages being around ~14–12 Ma [*Rolland et al*., 2009]. Fluid inclusion data indicate conditions of 375–385°C at 330–320 MPa [*Mullis*, 1996]. The clefts occurring in stage 2 shear zones are subvertical in orientation (Figures 2 and 3), with a rare intermediate cleft generation (Figure 2c) dipping at ~45° angle to the west. Rotated, old quartz veins consisting of centimeter-sized crystals often form competent layers in the country rock and act as incipient point for the formation of vertical clefts (Figure 3). Later stage 3 strike-slip deformation was likely weaker than the previous deformation phases and formed sinistral as well as dextral faults, showing chlorite and quartz crystallization. Dextral faults have an ENE-WSW orientation similar to stage 2 deformation. The WNW-ESE to NW-SE oriented sinistral faults are well developed just north of the monazite cleft area [see *Rolland et al*., 2009]. Fault gouge K-Ar ages covering the range from 10.5 to ~7 Ma [*Kralik et al*., 1992] likely date this deformation stage, *P-T* conditions decreased to at least ca. 330°C and

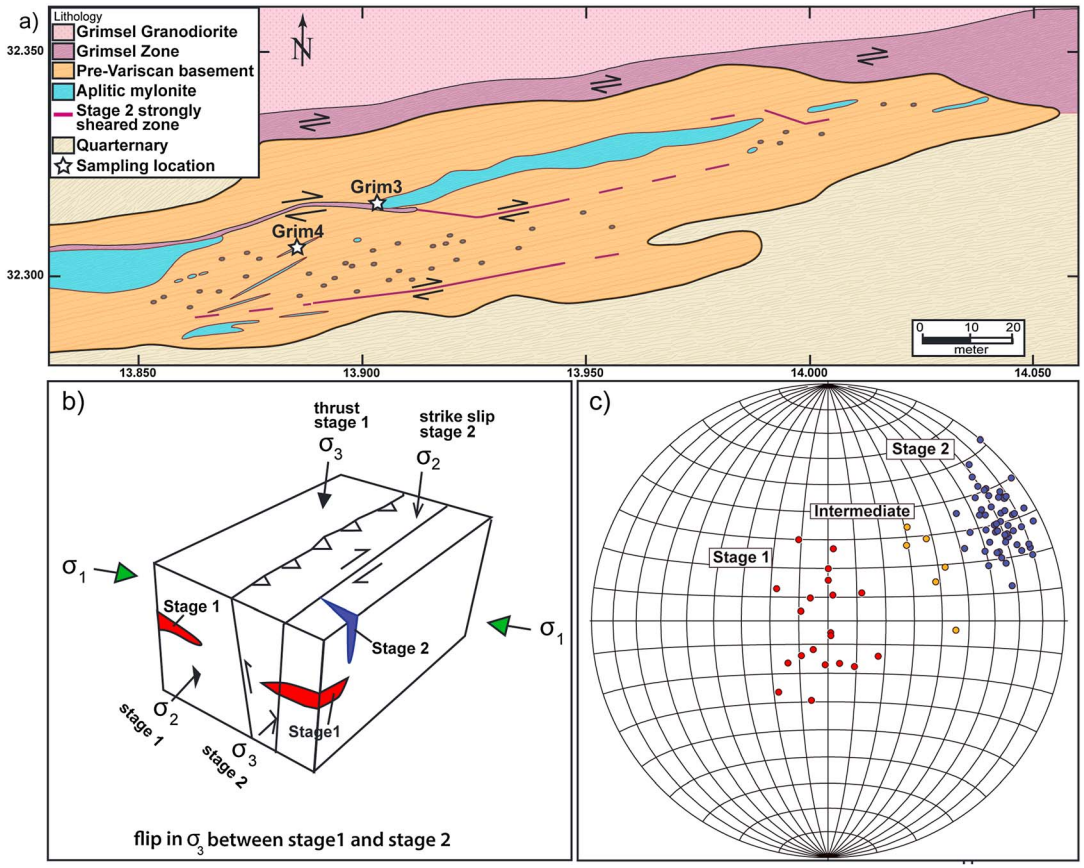

Figure 2. (a) Detailed map of the area between Lake Oberaar and the Oberaar Glacier (see Figure 1 for location). (b) Schematic representation of the two Grimsel area deformation stages and the formation of clefts in relation to these deformations. Stage 1 refers to the older horizontal cleft generation, while stage 2 refers to the younger vertical cleft generation. Note the switch in σ_2 and σ_3 between the two deformation phases. The rare intermediate cleft generation has a ~45° dip and formed during the transition between the two deformation stages. (c) Stereographic projection displaying cleft orientation data and deformation direction during cleft formation (equal area projection, lower hemisphere).

230 MPa [*Mullis*, 1996]. The youngest dated stage 4 deformation led to a brittle reactivation of ENE-WSW oriented shear zones with local hydrothermal brecciation at around 3.3 Ma [*Hofmann et al*., 2004; *Villa and Hanchar*, 2013].

The overall deformation structures are concentrated in a zone of highly variable crystalline basement units that separates the Grimsel Granodiorite gneisses to the north from the Southeastern Aare Granite gneisses to the south (Figure 1). The dominant rock types are orthogneisses, but meta-sedimentary and meta-volcanic rocks such as meta-rhyolite also occur in this so-called Grimsel-Zone [*Stalder*, 1964; *Oberhänsli et al*., 1988]. The southern portion of the Grimsel Granodiorite developed a border facies, which is rich in aplites [*Stalder*, 1964] (Figures 1 and 2). All of these units are intensively deformed and dissected by shear zones [*Rolland et al*., 2009; *Wehrens*, 2015].

3. Cleft Occurrence and Sampling Locations

The mechanics of cleft formation requires brittle failure of rocks, but they occur in and in direct vicinity of ductile shear zones (see section 1). Hydrothermal monazite is only occasionally reported to occur in Alpine clefts [e.g., *Parker*, 1954], and the authors collected the three monazite samples (PK2, GRIM3, and GRIM4) analyzed in this study in clefts of different orientation in the Lake Oberaar area (Figures 1–3 and Table S1 in the supporting information). The detailed structural relationships differ between the clefts, but the monazites PK2 (from a horizontal cleft), GRIM3, and GRIM4 (from vertical clefts) are from clefts related to brittle boudinage of competent layers in a fine-grained, mica-rich ductily deforming matrix. Mylonitic rocks, richer in micas, contain far fewer or nearly no clefts. In these mylonites, late chlorite-filled veins often form the

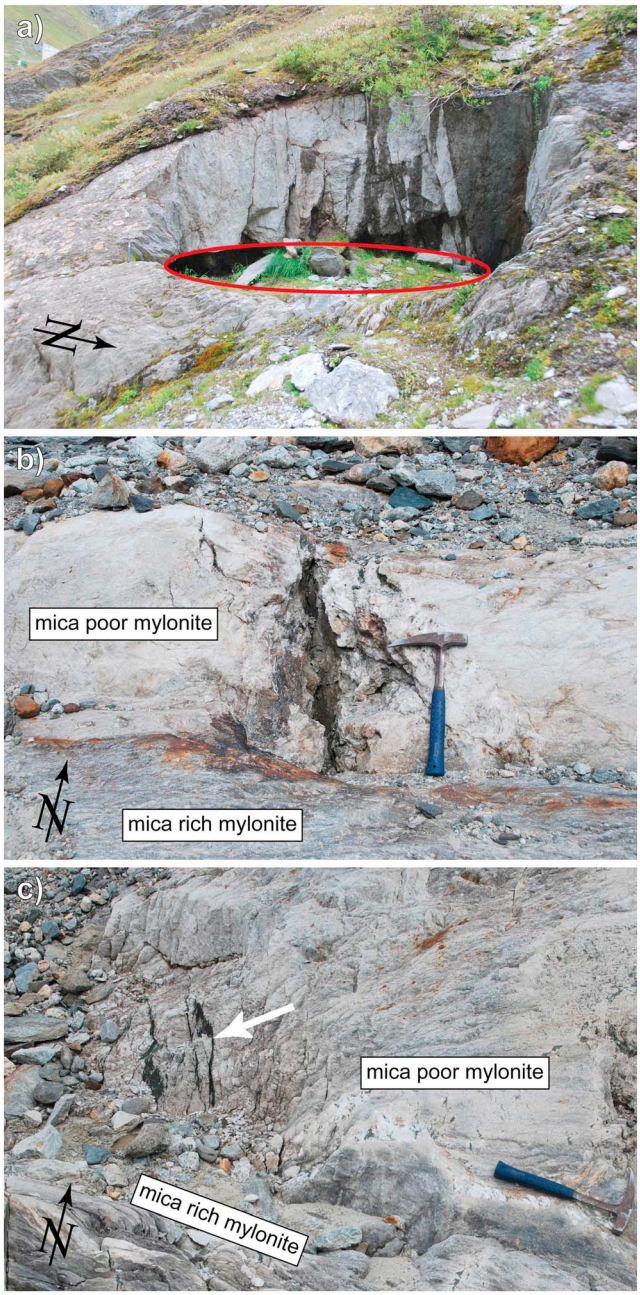

Figure 3. Cleft generations as observed in the field. Note that in all cases the cleft space is enlarged due to mineral extraction. (a) Several meters wide horizontal stage1 cleft (red elipse) in which monazite PK2 was sampled, located in the neck of a large scale boudinage structure. (b) Vertical stage 2 cleft that contained monazite GRIM4. (c) Vertical stage 2 cleft (white arrow) that contained monazite GRIM3, note the more strongly fractured appearance of the mica-poor mylonite. The two vertical clefts developed in the necks of boudins in more brittle deformed leucocratic mylonite forming a band within more ductile deformed schistose mylonite. Coordinates are given in Table S1.

lateral continuations of vertical boudinage clefts located in the rigid layers (Figure 3). The link between rock behavior and cleft occurrence shows the rheological control on cleft formation, as the mica-poor layers show brittle behavior while the more mica-rich mylonite shows more ductile behavior during deformation. The combination of rheology contrasts and fluid availability controls the development of clefts. This means that minerals crystallizing in clefts have the potential to record time and temperature of ductile-brittle deformation during regional tectonic events.

Monazite has in the past already rarely been found in horizontal stage 1 clefts [*Stalder*, 1964; *Dollinger*, 1989] but is otherwise not known from clefts of the Grimsel Granodiorite. The cleft hosting monazite sample PK2 is an example of such a horizontal cleft located in a stage 1 shear zone hosted in meta-rhyolite of the Grimsel Zone (Figures 1 and 3a). This cleft is ~3 m by 0.5 m and located in a boudin structure. The monazite is associated with adularia, quartz, chlorite, and accessory minerals (Table S1).

In contrast to the predominance of horizontal clefts in the Grimsel Granodiorite, vertical clefts are restricted to stage 2 shear zones and their immediate surroundings [*Rolland et al.*, 2009]. These clefts developed mainly in areas of competence contrast and boudinage of former aplitic material in paragneisses (for example, blue colored layers in Figure 2). Only recently, a phengite-chlorite shear zone containing a set of vertical clefts has become exposed west of Oberaar Lake by the retreating Oberaar glacier (Figure 1). Clefts hosting samples GRIM3 and GRIM4 are an example of such vertically oriented clefts. These two localities are ~40 m apart and occur in leucocratic granitic gneiss in a muscovite-rich mylonitic shear zone (Figures 1 and 2). GRIM4 is from a cleft a few centimeter wide located in a boudinaged leucocratic gneiss layer (Figure 3b). Cleft GRIM3 is $<$1 cm in width, several decimeters in lengths, and surrounded

by leached, porous country rock (Figure 3c). The mineral association in both clefts is monazite, quartz, chlorite, adularia or albite, and ilmenite.

4. Analytical Techniques

Monazite was identified in the laboratory by using the unfiltered light of a quarz-lamp (=mercury vapor lamp), which has intense visible emission lines at 577/579 nm [e.g., *Megger and Westfall*, 1950]. These lines are strongly absorbed by Nd in monazite, with the mineral then appearing bright green to blue-green and therefore easily detectable on hand-samples. Other cleft minerals were identified through an energy dispersive spectroscopy-equipped JEOL JSM7001F and a Zeiss DSM940A electron microscope at the University of Geneva and the Natural History Museum of Geneva. The three separated monazite grains were then polished down to the level of a central cross section, and backscatter electron (BSE) images were obtained. Growth domains visible in BSE images basically correlate with variations in Th concentrations, and these growth domains were used to place secondary ion mass spectrometry (SIMS) spot analyses (Figure 4) in order to capture the crystallization history. Measurement spots located near cracks or holes were avoided, as it was observed that the Th-Pb system could be disturbed in such areas, especially when interaction with hydrothermal fluids is expected [*Janots et al*., 2012; *Berger et al*., 2013].

Th-U-Pb analyses were carried out on three monazite crystals at the Swedish Museum of Natural History (NordSIM facility) on a Cameca IMS1280 SIMS instrument. Analytical methods closely followed those described by *Harrison et al*. [1995] and *Kirkland et al*. [2009], using a −13 kV O_2^- primary beam of ~6 nA and nominal 15 μm diameter. The mass spectrometer was operated at +10 kV and a mass resolution of ~4300($M/\Delta M$, at 10% peak height), with data collected in peak-hopping mode using an ion-counting electron multiplier. GRIM3 and GRIM4 U-Pb and Th-Pb data were calibrated against monazite standard 44069 [*Aleinikoff et al*., 2006]. PK2 U-Pb and Th-Pb data were calibrated against an in-house reference monazite, C83-32 [*Corfu*, 1988]. Analytical details and correction procedures closely follow those described in *Kirkland et al*. [2009] and *Janots et al*. [2012]. Lead isotope signals were corrected for common Pb contribution by using measured ^{204}Pb and an assumed present-day Pb isotope composition according to the model of *Stacey and Kramers* [1975]. Measurement of ^{204}Pb is subject to unresolvable molecular interference by $^{232}Th^{143}Nd^{16}O_2^{++}$ (also affecting ^{206}Pb and ^{207}Pb to a lesser degree through replacement of ^{16}O with heavier O-isotopes), which may result in an overestimation of common Pb concentrations. A correction was applied whenever the $^{232}Th^{143}Nd^{16}O_2^{++}$ signal at mass 203.5 exceeded the average background signal on the ion-counting detector by three times its standard deviation. Age calculations use the decay constants recommended by *Steiger and Jäger* [1977], and plots were done by using Isoplot v. 3.71 [*Ludwig*, 2009]. Th-Pb ages presented in the results section were corrected for common Pb and doubly charged $^{232}Th^{143}Nd^{16}O_2^{++}$-overlap and are given with 2σ uncertainties. After the SIMS analyses laser ablation-inductively coupled plasma-mass spectrometry (LA-ICP-MS) measurements were conducted at the University of Bern by using a Lambda Physik GeoLas pro 193 nm ArF Excimer laser system coupled with an Perkin Elmer ELAN-DRCe quadrupole ICP-MS. Measurements closely followed procedures from *Pettke et al*. [2012], employing an energy density of 4–5 J cm^{-1} on the sample surface at 10 Hz laser repetition rate and a spot diameters of 60 μm. Analysis points were placed next to ion probe age dating spots. The ICP-MS settings were optimized to maximum signal to background intensity ratios with $(^{232}Th^{16}O)^+$ production rates tuned to below 0.2% and robust plasma conditions as monitored by equal sensitivities of U and Th. Data reduction was done by using SILLS [*Guillong et al*., 2008] with improved calculation of the limit of detection [*Pettke et al*., 2012], by summing the major element oxide totals to 100% [e.g., *Gray*, 1985]. Synthetic SRM 610 glass from the National Institute of Standards and Technology was used as the external standard.

Doubly polished fissure quartz samples from the GRIM4 fissure were investigated by microthermometry using a Linkam Inc THMSG 600 freezing-heating stage. Calibration was done on synthetic fluid inclusion standards at temperatures of 0.0°C and 374.1°C (ice melting and critical homogenization, respectively) of pure water and at temperatures of −56.6°C and 10°C (CO_2 melting and H_2O-CO_2 clathrate dissociation, respectively). The temperature range between 100°C and 300°C was verified with appropriate chemicals from Merck corporation. Measurement precision between −30 and 40°C is ±0.1°C and ±1°C outside this range. Raman spectroscopy was performed on a Bruker Senterra system, using a wavelength of 532 nm. Analyses of representative fluid inclusions confirmed the presence of small amounts of CO_2 dissolved in aqueous

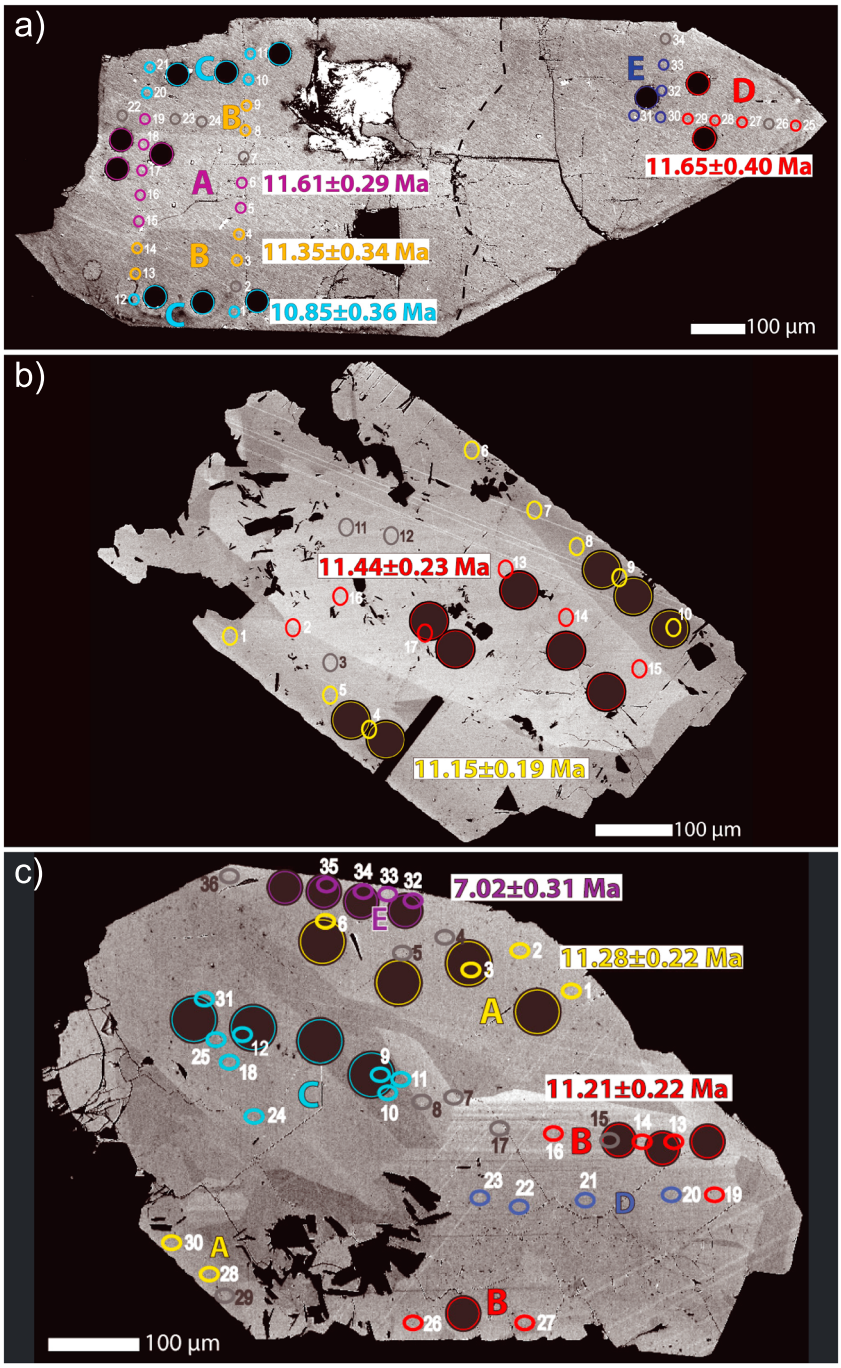

Figure 4. BSE images of monazite grains (a) PK2 (the light part within the grain is leftover gold coating), (b) GRIM4, and (c) GRIM3. The numbered circles indicate SIMS analysis points and are colored according to domains with pooled domain ages given in the respective color. The spots in grey were not included in the age calculations. The larger circles indicate LA-ICP-MS measurement points; colors indicate domains.

solution of inclusion populations 1 to 3. Volume fractions of the liquid and vapor phases in fluid inclusions were estimated by using the spindle stage technique at the University of Bern [*Bakker and Diamond*, 2006]. In gas-absent aqueous fluid inclusions, salinity was obtained from the ice melting temperature in NaCl-equivalents after *Potter et al.* [1978] and *Bodnar* [1993]. In the presence of CO_2-clathrate and CO_2-vapor, salinity was estimated from the melting temperature of ice by using the experimental data of *Bozzo et al.* [1973]. The concentration of dissolved CO_2 in aqueous solution was approximated by using Henry's law

constant of *Drummond* [1981] and the CO_2 fugacity at the pressure and temperature of clathrate dissociation. Isochores of fluid inclusion populations were constructed with reference to the system H_2O-CO_2-NaCl applying the equation of state of *Bowers and Helgeson* [1983], adapted in *Bakker* [1999], and presented in Loner B, Software Package Fluids, v.2 (modification 01/2012). The isochore of the inclusion population 4 only containing H_2O was confirmed by synthetic fluid inclusions of *Zhang and Frantz* [1987] and *Bodnar and Vityk* [1994]. The *P-T* domain of fluid inclusion formation is given by the intersection of fluid inclusion isochores at the lithostatic gradient of 30°C/km.

5. Results

5.1. Monazite Composition and Texture

Uranium and thorium concentrations obtained by SIMS are listed in Table 1, and chemical compositions of dated domains determined through LA-ICP-MS analyses are given in Table S2. The zoning patterns of the three analyzed crystals visible in BSE images differ greatly, with distinct chemical zones largely corresponding to the observable zonation, particularly in Th and U, but also in the REE patterns.

The monazite grain from sample PK2 (Figure 4a) shows an inner zone (zone A) surrounded by a relatively small incomplete inner rim (zone B) with a broader outer rim (zone C), separated by an irregularly shaped border from the pointed end of the crystal (zones D and E). Monazite PK2 contains 15,400–37,800 μg/g Th and 29–86 μg/g U, translating to Th/U ratios of 360–995. Th concentrations generally decrease from core to rim, while U increases from core/inner rim to outer rim. The pointed end of the crystal has a distinct composition with medium-high Th concentrations and the highest U concentrations in the crystal. LA-ICP-MS rare earth element patterns show groups C and D having the same light REE (LREE) pattern, and domain C has lower concentrations of the element range from Ho to Lu. Domain A has a distinct pattern with elevated medium REE (MREE) at lower LREE (see Figure S1 in the supporting information). Concentrations for Ca are 9300–16200 ppm, Sr 2900–5100, and Y 4300–9700 ppm.

In contrast, rim and core of GRIM4 (Figure 4b) are clearly distinguishable on BSE image as well as through Th and U contents. GRIM4 contains 14,500–45,800 μg/g Th and 84–220 μg/g U, returning Th/U ratios of 111–425. The core has high Th at low U concentrations, while the rim has low Th at higher U concentrations. LA-ICP-MS Th/U data lie between those of SIMS analyses, with higher U contents, indicating a mixed signal and therefore a more complicated structure at depth than visible on BSE images. Rare earth element patterns show a far less pronounced Eu anomaly compared to the other samples (see Figure S1). Concentrations for Ca are 2600–5900 ppm, Sr 1300–3000 ppm, and Y 5100–6200 ppm.

Sample GRIM3 shows complex zonation (Figure 4c) where five chemical zones (zones A to E) are distinguishable. GRIM3 contains 4600–34700 μg/g Th and 164–1230 μg/g U, returning Th/U ratios of 18–114. There is no clear trend in Th concentrations, but U is higher in the more porous, recrystallized areas of the crystal. LA-ICP-MS rare earth element patterns show a pronounced Eu anomaly. Domains A, C, and E have identical LREE patterns, while domains C and E have lower concentrations of the elements ranging from Sm to Tm. Domain B has a distinct pattern similar to domain A in PK2 with elevated MREE at lower LREE and HREE (see Figure S1). Concentrations for Ca are 2600–6100 ppm, Sr 1200–3200 ppm, and Y 5300–8600 ppm.

5.2. ^{232}Th-^{208}Pb Monazite Ages

Hydrothermal monazite is most reliably dated through ^{232}Th/^{208}Pb [e.g., *Janots et al*., 2012]. The U isotopic system is not usable due to low U concentrations resulting in unreliable ^{235}U-^{207}Pb ages. Additionally, the unquantifiable incorporation of ^{230}Th, a transitory decay product of the ^{238}U-^{206}Pb decay series, into the crystal lattice results in excess ^{206}Pb. When combined with a low amount of radiogenic Pb, higher common Pb fractions than observed in monazite from other environments and the young ages found, reliable U-Pb ages become difficult to determine (see detailed discussion in *Janots et al*. [2012]).

Measurement spots on crystal PK2 are located in the three distinguishable zones at one side of the crystal and at the free-grown crystal tip (Figure 4a). Based on the age results and chemical composition (Figures 5a and 5d), four growth domains (A–D) were identified (Figure 4a). Domain A located in the center and domain D at the tip of the crystal yield identical ages of 11.61 ± 0.29 Ma (mean square weighted deviation (MSWD) = 0.22) and 11.65 ± 0.40 Ma (MSWD = 0.20), respectively. Domain B, surrounding domain A, gives an age of 11.35 ± 0.34 Ma (MSWD = 0.55), and domain C, surrounding domain B, yields an age of 10.85 ± 0.36 Ma

AGU Tectonics

10.1002/2016TC004407

Table 1. Ion Microprobe U-Th-Pb Isotope Ratios and ^{232}Th-^{208}Pb Ages[a]

Sample	Analysis ID	U (ppm)	Th (ppm)	Th/U (meas)	$^{204}Pb/^{208}Pb$	±σ (%)	$^{232}Th^{143}Nd^{16}O_2^{2+}$ (/^{208}Pb)	±σ (%)	f208	±σ (abs.)	$^{232}Th/^{208}Pb$ (Uncorr.)	±σ (%)	$^{232}Th/^{208}$ Pb Age corrected (Ma)	±σ (Ma)
							PK2							
Group	n4192-PK2@05	50	33,737	679	0.00399	4.6	0.000269	15	0.13	0.01	0.00066	2.9	11.49	0.38
A	n4192-PK2@06	54	37,773	695	0.00353	3.7	0.000330	17	0.11	0.01	0.00065	2.8	11.57	0.37
	n4192-PK2@07	52	35,621	690	0.00386	4.0	0.000271	18	0.13	0.01	0.00067	2.9	11.72	0.39
	n4192-PK2@15	49	35,458	723	0.00386	3.5	0.000316	13	0.13	0.01	0.00067	2.9	11.74	0.39
	n4192-PK2@16	53	36,425	688	0.00368	4.4	0.000247	15	0.12	0.01	0.00066	2.8	11.77	0.38
	n4192-PK2@17	55	37,078	678	0.00391	4.6	0.000313	13	0.13	0.01	0.00067	2.8	11.76	0.38
	n4192-PK2@18	48	37,381	787	0.00450	3.3	0.000239	15	0.16	0.01	0.00069	2.9	11.67	0.40
	n4192-PK2@19	46	37,665	812	0.00566	2.9	0.000168	19	0.21	0.01	0.00070	2.9	11.26	0.40
	n4192-PK2@22	*52*	*41,000*	*782*	*0.00508*	*4.1*	*0.000108*	*36*	*0.19*	*0.01*	*0.00067*	*2.9*	*10.89*	*0.39*
	n4192-PK2@23	*50*	*34,411*	*693*	*0.00498*	*4.8*	*0.000067*	*45*	*0.19*	*0.01*	*0.00054*	*2.9*	*8.94*	*0.32*
Group	n4192-PK2@03	33	24,209	743	0.00807	3.1	0.000150	27	0.30	0.01	0.00077	2.9	10.83	0.45
B	n4192-PK2@04	34	26,252	778	0.00576	3.4	0.000216	19	0.21	0.01	0.00072	2.9	11.60	0.43
	n4192-PK2@08	29	29,247	995	0.00489	3.7	0.000238	21	0.17	0.01	0.00068	2.9	11.40	0.39
	n4192-PK2@09	31	28,937	936	0.00521	4.7	0.000203	20	0.19	0.01	0.00071	2.9	11.73	0.41
	n4192-PK2@13	32	25,765	801	0.00841	2.9	0.000188	20	0.31	0.01	0.00080	2.9	11.16	0.47
	n4192-PK2@14	30	27,421	917	0.00511	3.7	0.000158	21	0.19	0.01	0.00068	2.8	11.27	0.39
	n4192-PK2@24	*37*	*30,285*	*823*	*0.00501*	*4.8*	*0.000127*	*30*	*0.18*	*0.01*	*0.00060*	*2.8*	*9.87*	*0.34*
Group	n4192-PK2@1	36	19,711	547	0.00549	4.7	0.000134	28	0.20	0.01	0.00065	2.9	10.47	0.38
C	*n4192-PK2@02*	*10*	*18,143*	*1,773*	*0.00829*	*3.6*	*0.000159*	*28*	*0.31*	*0.01*	*0.00077*	*2.9*	*10.84*	*0.46*
	n4192-PK2@10	33	20,500	614	0.00846	3.1	0.000126	29	0.32	0.01	0.00084	2.9	11.47	0.49
	n4192-PK2@11	37	17,439	467	0.00855	3.5	0.000114	26	0.32	0.01	0.00079	2.9	10.83	0.45
	n4192-PK2@12	42	17,884	430	0.00896	4.1	0.000207	22	0.33	0.01	0.00083	3.0	11.25	0.50
	n4192-PK2@20	38	20,221	526	0.00891	3.2	0.000235	20	0.33	0.01	0.00081	2.9	10.92	0.47
	n4192-PK2@21	29	15,440	537	0.00753	4.1	0.000182	31	0.28	0.01	0.00072	2.9	10.55	0.42
Group	n4192-PK2@25	86	30,866	360	0.00412	3.7	0.000210	18	0.14	0.01	0.00068	2.8	11.72	0.39
D	*n4192-PK2@26*	*114*	*31,385*	*276*	*0.00456*	*3.9*	*0.000198*	*20*	*0.16*	*0.01*	*0.00070*	*2.8*	*11.85*	*0.40*
	n4192-PK2@27	80	32,083	400	0.00535	3.6	0.000211	21	0.19	0.01	0.00072	2.8	11.75	0.41
	n4192-PK2@28	80	30,979	387	0.00562	3.6	0.000116	32	0.21	0.01	0.00071	2.9	11.37	0.41
	n4192-PK2@29	75	32,288	429	0.00577	3.5	0.000110	29	0.21	0.01	0.00074	2.8	11.74	0.42
Group	*n4192-PK2@30*	*61*	*30,713*	*503*	*0.00628*	*3.5*	*0.000114*	*23*	*0.23*	*0.01*	*0.00077*	*2.8*	*11.92*	*0.44*
E	*n4192-PK2@31*	*65*	*37,585*	*579*	*0.00512*	*3.4*	*0.000137*	*22*	*0.19*	*0.01*	*0.00072*	*2.8*	*11.82*	*0.41*
	n4192-PK2@32	*57*	*22,162*	*392*	*0.00712*	*3.5*	*0.000165*	*25*	*0.26*	*0.01*	*0.00079*	*2.9*	*11.81*	*0.46*
	n4192-PK2@33	*57*	*25,651*	*447*	*0.00639*	*3.5*	*0.000211*	*20*	*0.23*	*0.01*	*0.00074*	*2.9*	*11.42*	*0.43*
	n4192-PK2@34	*13*	*17,638*	*1,389*	*0.00568*	*4.4*	*0.000205*	*25*	*0.20*	*0.01*	*0.00068*	*2.9*	*10.99*	*0.40*
							GRIM4							
Core	n4841mnz(Grim4)_@02	102	43,425	425	0.00100	6.1	0.000251	13	0.02	0.00	0.00057	2.5	11.35	0.28
	n4841mnz(Grim4)_@03	*84*	*31,863*	*381*	*0.00084*	*8.5*	*0.000262*	*17*	*0.01*	*0.00*	*0.00054*	*2.5*	*10.74*	*0.26*
	n4841mnz(Grim4)_@11	*197*	*33,098*	*168*	*0.00106*	*6.5*	*0.000257*	*15*	*0.02*	*0.00*	*0.00058*	*2.5*	*11.38*	*0.28*
	n4841mnz(Grim4)_@12	*217*	*40,333*	*186*	*0.00097*	*7.1*	*0.000271*	*15*	*0.02*	*0.00*	*0.00055*	*2.5*	*10.84*	*0.27*
	n4841mnz(Grim4)_@13	124	39,958	322	0.00095	6.1	0.000326	11	0.01	0.00	0.00057	2.5	11.42	0.28
	n4841mnz(Grim4)_@14	108	38,564	358	0.00099	6.0	0.000320	12	0.01	0.00	0.00059	2.5	11.69	0.29
	n4841mnz(Grim4)_@15	101	45,352	451	0.00097	5.7	0.000282	11	0.02	0.00	0.00059	2.5	11.66	0.29
	n4841mnz(Grim4)_@16	123	45,771	373	0.00095	5.9	0.000278	12	0.02	0.00	0.00058	2.5	11.60	0.28
	n4841mnz(Grim4)_@17	121	45,620	376	0.00095	6.1	0.000273	12	0.02	0.00	0.00055	2.5	10.97	0.27
Rim	n4841mnz(Grim4)_@1	181	14,531	80	0.00102	10.5	0.000338	20	0.01	0.00	0.00057	2.5	11.43	0.28
	n4841mnz(Grim4)_@04	127	21,432	169	0.00089	9.3	0.000196	22	0.02	0.00	0.00058	2.5	11.43	0.28
	n4841mnz(Grim4)_@05	127	17,823	141	0.00083	10.7	0.000207	24	0.02	0.00	0.00054	2.5	10.76	0.27

AGU Tectonics

10.1002/2016TC004407

Table 1. (continued)

Sample	Analysis ID	U (ppm)	Th (ppm)	Th/U (meas)	$^{204}Pb/^{208}Pb$	±σ (%)	$^{232}Th^{143}Nd^{16}O_2^{2+}$ (/^{208}Pb)	±σ (%)	f208	±σ (abs.)	$^{232}Th/^{208}Pb$ (Uncorr.)	±σ (%)	$^{232}Th/^{208}$ Pb Age corrected (Ma)	±σ (Ma)
	n4841mnz(Grim4)_@06	170	19,034	112	0.00100	9.6	0.000166	26	0.03	0.00	0.00056	2.5	11.07	0.27
	n4841mnz(Grim4)_@07	161	18,862	117	0.00094	9.9	0.000255	21	0.02	0.00	0.00057	2.5	11.26	0.28
	n4841mnz(Grim4)_@08	165	20,052	121	0.00089	10.4	0.000244	22	0.02	0.00	0.00055	2.5	10.94	0.27
	n4841mnz(Grim4)_@09	190	21,001	111	0.00090	10.3	0.000255	21	0.02	0.00	0.00055	2.5	10.96	0.27
	n4841mnz(Grim4)_@10	139	20,343	146	0.00109	8.8	0.000282	19	0.02	0.00	0.00058	2.5	11.38	0.28
							GRIM3							
Group	n4842mnz(Grim3)_@1	217	19,788	91	0.00120	7.3	0.000414	14	0.02	0.00	0.00058	2.5	11.57	0.29
A	n4842mnz(Grim3)_@02	175	20,075	114	0.00119	7.2	0.000420	13	0.01	0.00	0.00056	2.5	11.18	0.28
	n4842mnz(Grim3)_@03	265	19,486	74	0.00100	9.0	0.000381	16	0.01	0.00	0.00055	2.5	11.05	0.27
	n4842mnz(Grim3)_@04	*210*	*15,661*	*75*	*0.00157*	*7.4*	*0.000198*	*23*	*0.05*	*0.00*	*0.00051*	*2.5*	*9.91*	*0.24*
	n4842mnz(Grim3)_@05	*304*	*20,128*	*66*	*0.00115*	*9.2*	*0.000280*	*20*	*0.02*	*0.00*	*0.00051*	*2.5*	*9.97*	*0.25*
	n4842mnz(Grim3)_@06	168	14,115	84	0.00129	8.6	0.000413	17	0.02	0.01	0.00059	2.5	11.66	0.29
	n4842mnz(Grim3)_@28	274	19,138	70	0.00114	8.0	0.000357	16	0.02	0.00	0.00049	2.5	11.27	0.28
	n4842mnz(Grim3)_@30	277	18,265	66	0.00100	8.6	0.000304	17	0.02	0.00	0.00037	2.8	11.03	0.27
Group	n4842mnz(Grim3)_@13	422	34,685	82	0.00134	4.9	0.000412	10	0.02	0.00	0.00043	2.5	11.57	0.28
B	n4842mnz(Grim3)_@14	537	32,330	60	0.00116	6.1	0.000360	12	0.02	0.00	0.00057	2.5	10.70	0.26
	n4842mnz(Grim3)_@15	606	29,394	48	0.00105	7.1	0.000281	15	0.02	0.00	0.00057	2.5	10.12	0.25
	n4842mnz(Grim3)_@16	545	28,674	53	0.00132	5.9	0.000360	12	0.02	0.00	0.00036	3.6	11.23	0.27
	n4842mnz(Grim3)_@17	*539*	*28,570*	*53*	*0.00253*	*4.4*	*0.000327*	*13*	*0.07*	*0.00*	*0.00058*	*2.5*	*10.59*	*0.25*
	n4842mnz(Grim3)_@19	540	27,962	52	0.00123	6.1	0.000319	13	0.02	0.00	0.00041	2.7	11.34	0.28
	n4842mnz(Grim3)_@26	403	34,041	85	0.00121	5.7	0.000332	12	0.02	0.00	0.00059	2.6	11.29	0.28
	n4842mnz(Grim3)_@27	331	30,951	94	0.00239	4.4	0.000354	13	0.07	0.00	0.00046	2.6	11.18	0.28
Group	*n4842mnz(Grim3)_@07*	*214*	*42,112*	*197*	*0.00156*	*4.4*	*0.000354*	*10*	*0.03*	*0.00*	*0.00041*	*2.5*	*11.67*	*0.28*
C	*n4842mnz(Grim3)_@08*	*397*	*26,465*	*67*	*0.00079*	*10.5*	*0.000259*	*20*	*0.01*	*0.00*	*0.00057*	*2.5*	*9.80*	*0.24*
	n4842mnz(Grim3)_@09	234	8,401	36	0.00153	11.2	0.000206	33	0.04	0.01	0.00051	2.5	10.96	0.27
	n4842mnz(Grim3)_@10	340	6,543	19	0.00061	33.4	0.000246	58	0.01	0.01	0.00048	3.0	7.37	0.21
	n4842mnz(Grim3)_@11	174	4,596	26	0.00128	13.8	0.000146	45	0.04	0.01	0.00060	2.5	9.29	0.27
	n4842mnz(Grim3)_@12	259	10,719	41	0.00126	9.9	0.000372	20	0.02	0.01	0.00057	2.5	11.62	0.29
	n4842mnz(Grim3)_@18	451	13,337	30	0.00074	17.7	0.000140	45	0.02	0.01	0.00051	2.5	8.60	0.22
	n4842mnz(Grim3)_@24	380	12,789	34	0.00111	11.8	0.000187	32	0.03	0.01	0.00052	2.6	9.93	0.25
	n4842mnz(Grim3)_@25	*288*	*7,549*	*26*	*0.00136*	*11.9*	*0.000302*	*28*	*0.03*	*0.01*	*0.00059*	*2.5*	*10.15*	*0.27*
	n4842mnz(Grim3)_@31	296	6,259	21	0.00093	19.7	0.000087	71	0.03	0.01	0.00043	2.5	8.05	0.20
Group	n4842mnz(Grim3)_@20	1,225	21,596	18	0.00077	16.9	0.000186	38	0.02	0.01	0.00055	2.5	7.17	0.26
D	n4842mnz(Grim3)_@21	876	21,391	24	0.00082	13.2	0.000188	30	0.02	0.00	0.00057	2.5	8.53	0.22
	n4842mnz(Grim3)_@22	896	20,946	23	0.00101	11.1	0.000179	29	0.03	0.00	0.00057	2.5	9.04	0.23
	n4842mnz(Grim3)_@23	1053	18,879	18	0.00154	10.8	0.000130	41	0.05	0.01	0.00046	2.5	7.90	0.21
Group	n4842mnz(Grim3)_@32	249	16,166	65	0.00607	6.0	0.000077	58	0.23	0.01	0.00043	2.6	6.75	0.17
E	n4842mnz(Grim3)_@34	175	16,714	95	0.00840	4.1	0.000096	41	0.32	0.01	0.00051	2.8	7.04	0.17
	n4842mnz(Grim3)_@35	164	15,988	97	0.00723	4.4	0.000146	33	0.27	0.01	0.00048	2.5	7.09	0.16
	n4842mnz(Grim3)_@33	210	15,794	75	0.00292	8.5	0.000124	45	0.10	0.01	0.00040	2.6	7.21	0.18
	n4842mnz(Grim3)_@36	*139*	*15,424*	*111*	*0.00175*	*7.3*	*0.000355*	*18*	*0.04*	*0.01*	*0.00055*	*2.5*	*10.60*	*0.27*

[a]Measurement data given in italic were excluded from the interpretation

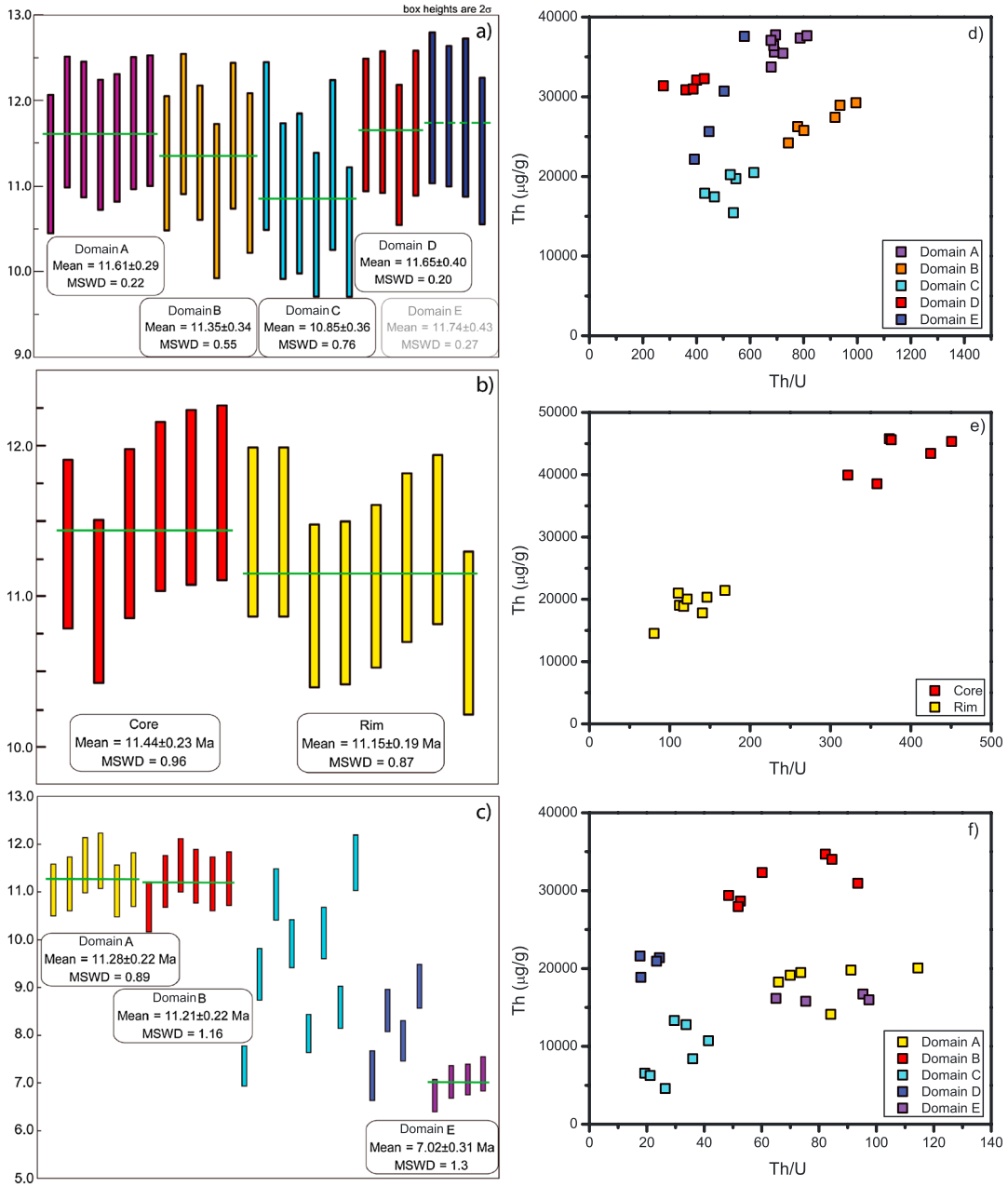

Figure 5. ^{232}Th-^{208}Pb SIMS ages of (a) PK2, (b) GRIM4, and (c) GRIM3. Compositional variation in cleft monazite ion probe data. Th versus Th/U plots of the Grimsel area monazites with (d) PK2, (e) GRIM4, and (f) GRIM3.

(MSWD = 0.76). This means that mean values tend to decrease from core to rim (zones A to C), but ages overlap within 2σ standard deviation. The domain B Th-U contents, although distinct, show a trend toward domain C values. Domain E data points have been separated because they are compositionally heterogeneous. Moreover, domain E gives an average age of 11.74 ± 0.43 Ma (MSWD = 0.27), which again overlaps with the ages of the other domains. Analysis spots 02, 07, 22–24, 26, and 34 were excluded due to their location on fractures or holes.

Crystal GRIM4 shows a simple division into core and rim in the BSE image (Figure 4b). This division is reflected in a markedly higher Th contents in the core of 38,600–45,800 when compared to 14,500–21,400 µg/g Th in the rim (Figure 5e). The Th-Pb ages for both regions (Figure 5b) overlap (core: 11.44 ± 0.23 Ma, MSWD = 0.96); rim: 11.15 ± 0.19 Ma, MSWD = 0.53). Analysis spots 03, 11, and 12 were excluded due to their location on fractures or holes and signs of possible alteration.

Table 2. Fluid Inclusion Data of Quartz From GRIM4 Cleft

HM	FP	IT	nI	VoT	V% Bubble	Daugh Mineral	Tm_{Ice}	Td_{Clathr}	Th_{Incl}	H_2O	NaCl	CO_2	*T* (°C)	*P* (MPa)
(1)	(2)	(3)	(4)	(5)	(6)	(7)	(8)	(9)	(10)	(11)	(12)	(13)	(14)	(15)
Tect.Qtz early	1	I	20	H_2O	9 ± 1	Rt, A	-6.0−6.1/−5.9	−6.05.0/7.0	206199/209	95.5	2.5	2.0	366 ± 22	316 ± 20
Qtz interm.	2	II	16	H_2O	8.5 ± 1	Rt, A	-3.8−3.8/−3.7	5.75.0/6.5	197190/201	96.6	1.4	2.0	344 ± 20	294 ± 18
Qtz interm.	3	II	14	H_2O	8 ± 1	Rt, A	-3.6−3.7/−3.5	4.13.5/5.0	187183/191	97.1	1.2	1.7	325 ± 19	279 ± 18
Qtz late	4	II	7	H_2O	6 ± 1	n.o.	−1.7−1.8/−1.6	n.o.	160155/166	99.0	1.0	~0	294 ± 18	252 ± 17

Crystal GRIM3 exhibits a complex, sector to patchwork-zone growth pattern (Figure 4c). Growth domains in the center and along the rim of the grain were chosen for analysis. With respect to measurement spot 3locations and growth domain pattern, the data set is divided into five domains (A-E; Figure 4c). Two distinct age groups can be identified for the entire data set (Figure 5c). The oldest group encompasses identical ages of 11.28 ± 0.22 Ma, MSWD = 0.89 (domain A) and 11.21 ± 0.22 Ma, MSWD = 1.16 (domain B). The youngest group (domain E) returns an age of 7.02 ± 0.31 Ma, MSWD = 1.3. Despite giving a well-defined and distinct age, this younger domain E is chemically indistinguishable from the adjacent domain A (Figure 5f) to which it has a lobate border, visible on the zoomed in BSE image. Domains C and D show distinct and internally consistent U-Th abundance patterns. However, these domains do not yield reliable mean ages but instead cover the entire age range of the crystal (domain C: 11.62–7.37 Ma; domain D: 9.04–7.17 Ma). Analysis spots 04, 05, 07, 08, 15, 17, and 29 were excluded due to their location on fractures or holes, while analysis spot 36 was excluded due to its location on a domain border.

5.3. Fluid Inclusions

Four fluid inclusion populations have been found in quartz crystals from the monazite-bearing vertical cleft GRIM 4 (Table 2). The earliest inclusion population is of pseudosecondary nature, whereas all others, with decreasing age, are of secondary nature. Carbon dioxide is present at room temperature in the vapor state and its content decreases from around 2 mol % in the earliest to ~0 mol % in the youngest fluid inclusion population. Salt as NaCl equivalents dissolved in the aqueous solution decreases also with time from around 2.5 mol % to 1 mol %. In addition, the mean values of the total homogenisation temperatures decrease from 206 to 160°C (Figure 6).

Temperatures and pressures deduced by intersection of the estimated lithostatic geothermal gradient (30°C/km, according to *Mullis* [1996]) with the isochores of the fluid inclusion populations yield mean values of 366°C at 316 MPa for the earliest population, and 344°C, 325°C, and 294°C at 294 MPa, 279 MPa, and 252 MPa for population 2 to 4, respectively (Table 2).

6. Discussion

Cleft formation documents the onset of brittle deformation that occurs in the study region different episodes at around 450–330°C [*Mullis*, 1996] in a specific, lithologically heterogeneous unit undergoing variably localized deformation during the retrograde evolution. The normal to the cleft plane provides the orientation of σ_3, and the cleft mineralogy and fluid inclusion data help constrain the temperature and fluid chemistry during mineralization. Cleft mineral and monazite crystallization may also occur during younger brittle deformation stages of different orientation. As demonstrated here, precise and accurate age data can be obtained for multiple stages of hydrothermal monazite crystallization as revealed by BSE imaging, thus allowing for precise age constraints on prominent changes in deformation regime during unroofing of orogens. Such robust monazite crystallization ages (combined with other data) thus greatly improve our understanding of the retrograde temperature-deformation-time (*T-D-t*) path.

6.1. *P-T* Conditions in the Grimsel Area

The silica content in white mica is the preferred measure of Tschermak substitution and used for phengite geobarometry [e.g., *Massone and Schreyer*, 1987, 1989]. Peak pressure conditions used for recent *P-T-t* models of the Grimsel area shear zones [*Challandes et al*., 2008; *Goncalves et al*., 2012] were estimated at ~600–650 ± 100 MPa through phengite geobarometry. Here we interpret these data as maximum pressure estimates, for the following reason. Plotting the "phengite" analyses of *Challandes et al*. [2008] and *Goncalves*

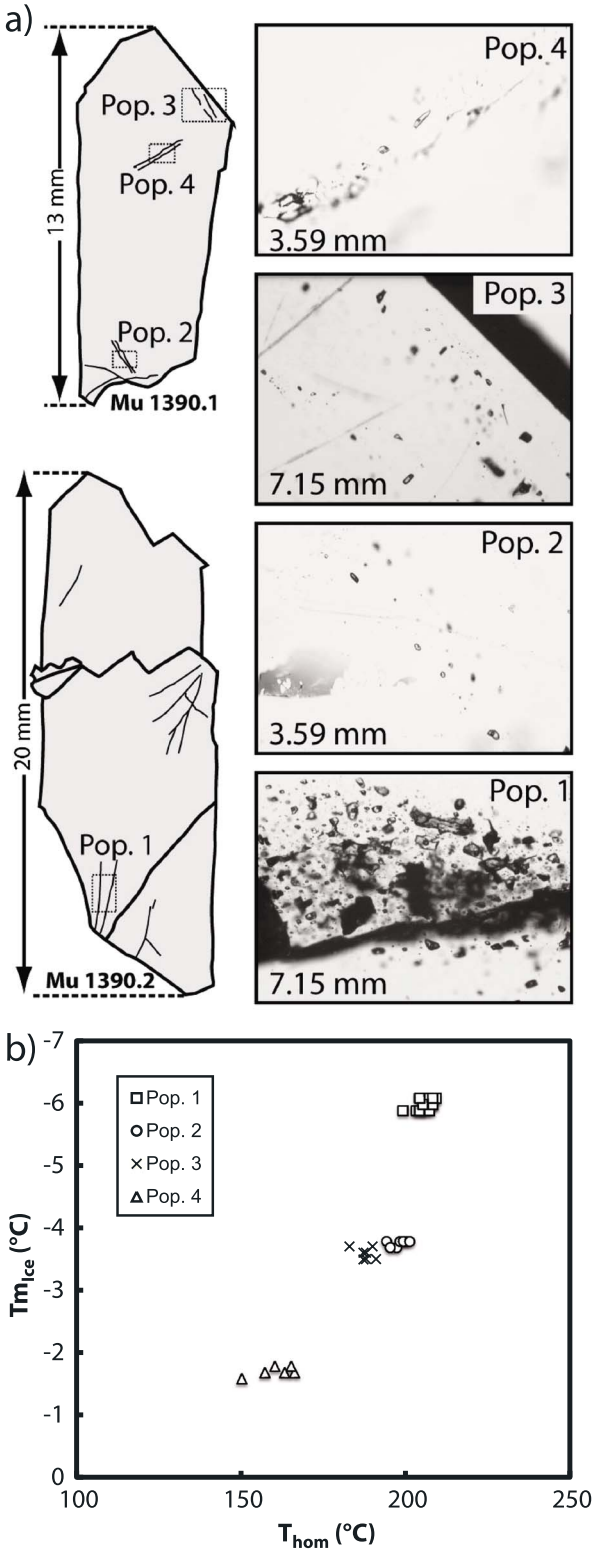

Figure 6. (a) Locations of fluid inclusion populations (populations 1–4) in two doubly-polished quartz crystal selected for analysis. Millimeters indicate image width. (b) Melting temperature of ice (Tm_{Ice}) versus total homogenization temperature (*T*) of the four GRIM4 quartz fluid inclusion populations. Population 1 is equivalent to population 2 at the Zinggenstock site (for location see Figure 1 [*Mullis*, 1995, 1996]).

et al. [2012] from the Grimsel shear zones in the diagram proposed by *Giudotti* [1984] (Figure 7), it can be seen that the white micas plot on the muscovite-ferriphengite trend. In contrast to a Tschermak substitution (muscovite-phengite trend) the cell volume increases with increasing Fe^{3+} [*Giudotti*, 1984]. If an ideal Tschermak substitution is assumed, the content of divalent iron can be estimated as (Si-6)-Mg (based on 22 charges per formula unit). This indicates for these data sets that iron is predominantly ferric and not ferrous. Hence, the elevated Si content in the white mica is not simply due to a Tschermak exchange (Mg content) but also due to an illite-type exchange $K^{XIII} + Al^{IV} = []^{XIII} + Si^{IV}$, leading to a slight K deficiency. This leads to an overestimation pressure conditions, meaning that the 440 MPa obtained independently by studying primary fluid inclusions in cleft quartz is likely a better estimate [*Mullis*, 1996]. The pressure estimate of 440 MPa is therefore also representative of stage 1 deformation [*Rolland et al*., 2009].

The microthermometric study of *Mullis* [1996] revealed three fluid inclusion generations related to three well-defined quartz generations from a large cleft system located at the Zinggenstock (Figure 1), in the vicinity of the monazite-bearing clefts studied. The earliest fluid inclusion population records conditions of 450°C and 440 MPa, the second population, associated with cleft monazite occurrence [*Mullis*, 1995], formed at around 375–385°C at 330–320 MPa and the latest at ~330°C and 230 MPa. The mineral parageneses contemporaneously included in the three quartz generations reflect biotite stability conditions for the first, chlorite stability for the second, and white mica (phengite) stability for the third quartz generation and fluid inclusion populations [*Mullis*, 1995]. The

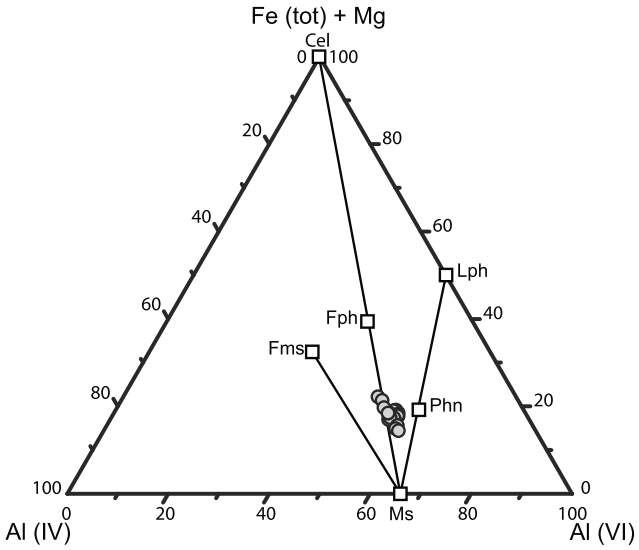

Figure 7. (Fe_{tot}) + Mg)-Al^{IV}-Al^{VI} ternary diagram for white mica [after *Giudotti*, 1984]. Data of *Challandes et al.* [2008] plot on the muscovite-ferriphengite trend. Previously assumed muscovite-phengite pressure estimates therefore represent only maximum pressure conditions. Abbreviations: Cel, celadonite; Lph, lithiophyllite; Phn, phengite; Fph, ferriphengite; Fms, ferrimuscovite; Ms, muscovite.

Zinggenstock cleft system affected by stage 1 to stage 3 deformations is >40 m in length and oriented ~340–350 strike/50–80 dip.

The pseudosecondary fluid inclusions in quartz from the vertical GRIM 4 cleft (Figures 6 and 9 and Table 2) permit this cleft formation stage to be attributed toward the end of the second fluid inclusion population documented at the Zinggenstock site [*Mullis*, 1995, 1996] and hence to stage 2 deformation at conditions of ~370°C and 320–330 MPa. The GRIM 4 quartz crystals of this vertical cleft also contain three additional sets of secondary fluid inclusion populations (Table 2) indicative of continuing activity along these shear zones at temperatures as low as ~290°C.

6.2. Monazite Composition

Thorium concentrations (Table 1) of the analyzed monazite crystals are similar to other dated Alpine cleft monazites [*Gasquet et al*., 2010; *Janots et al*., 2012; *Berger et al*., 2013; *Gnos et al*., 2015]. Uranium concentrations are very low, as seems to be characteristic for hydrothermal cleft monazite [e.g., *Catlos*, 2013; *Janots et al*., 2012], with the lowest values reported for highly oxidizing conditions [*Gnos et al*., 2015]. The high Th/U ratios of 360–995 of monazite PK2 (horizontal cleft), along with hematite and senaite in the cleft, therefore reflect the highly oxidizing conditions in this cleft. Under these conditions, U occurs partially as U^{6+} and therefore cannot be accommodated in the monazite structure [*Janots et al*., 2012; *Gnos et al*., 2015]. Lower Th/U ratios for GRIM4 (vertical cleft) of 80–425 and GRIM3 (vertical cleft) of 19–114 reflect less oxidizing conditions than in the horizontal PK2 cleft, as also reflected in the association of monazite with Fe^{2+}-bearing ilmenite instead of hematite (Table S1).

As LA-ICP-MS Th/U concentrations of the two GRIM4 zones, lying between those of SIMS analyses, suggest a more complex structure at depth than visible on the BSE image, no link can be made between compositional and age data for this sample. The two domains B (in GRIM3) and A (in PK2) are the only ones with Si contents above detection limit, the highest Th concentrations within each of those grains and show lowered La (and PK2 also Ce) contents at elevated MREE. Combined with prominent variations in Th/U ratios between these and other growth domains of within error identical age, this suggests variations in fluid chemistry during successive monazite growth stages which can be speculated to stem from dissolution of different wall rock minerals (e.g., allanite compared to monazite). The other age domains of GRIM3 and PK2 show identical LREE patterns for each grain (Figure S1). However, the youngest domains of these grains, especially in PK2, diverge toward lower concentrations from Sm to Tm (domain E in GRIM3) and Ho to Lu

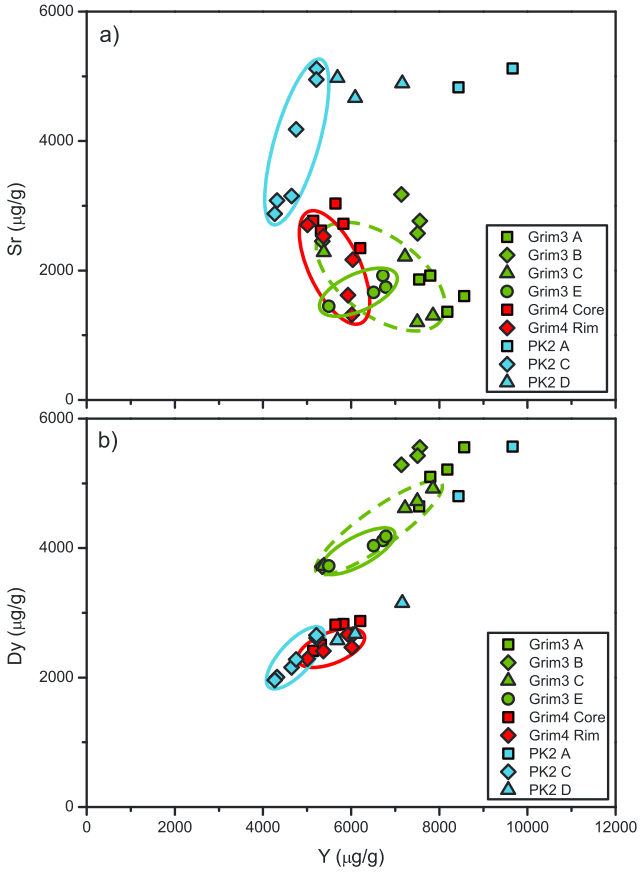

Figure 8. Selected trace element diagrams. The colored ellipses mark the youngest/outer zones in each grain, with the dashed ellipsis marking a zone giving mixed ages and showing signs of recrystallization.

(domain C in PK2; Figures S1 and 8a). Additionally, in both grain contents of Y, in PK2 also Ca/Sr and Th/U are lowered (Figures 5d–5f and 8b), in GRIM3 the U content is elevated in the youngest age domains.

6.3. Monazite Age Data

Age data available for the Grimsel area are compiled in Figure 9, which illustrates the timing of near peak and retrograde *P-T-t* evolution in the Grimsel area. Ages obtained for hydrothermal cleft adularia in the Grimsel area are between 11.51 ± 0.42 Ma and ~11.5–14.5 Ma (^{40}Ar-^{39}Ar ages [*Rossi and Rolland*, 2014; *Rauchenstein-Martinek*, 2015]) and were interpreted as crystallization or cooling ages, which overlap with or slightly predate monazite crystallization dated in this study. The oldest monazite Th-Pb domain age of 11.65 ± 0.40 Ma (horizontal cleft; sample PK2) indicates that monazite crystallization in the Grimsel zone is coeval with adularia crystallization. The older parts of monazite of the vertical clefts are comparable in age (11.44 ± 0.23 to 11.15 ± 0.19 Ma), whereas formation of the rim zone on monazite GRIM3 is 4 Ma younger at 7.02 ± 0.31 Ma (zone E; Figure 4c). This age zone displays an irregularly lobate boundary toward the adjacent zone A. This texture and an identical chemical composition of the two zones suggest partial dissolution-reprecipitation reactions, whereby zones C and D (Figures 5c and 5f) with uniformly low Th/U ratios may represent mixtures of these two domains, which are separated by around 4 Ma. The two zones contain micropores which have been found to be indicative of recrystallization processes in monazite and other minerals [e.g., *Putnis*, 2002, 2009]. Growth domains unaffected by dissolution-reprecipitation do not undergo (diffusional) modification of the Th-Pb systematics as shown by the tight clustering of older age populations of this monazite crystal and, hence, the older crystallization ages remain intact [*Seydoux-Guillaume et al*., 2002].

6.4. Timing and Tectonic Implications

Most early K/Ar ages on rock minerals from the general region were produced to constrain the cooling history and sampled without structural context. These ages show a large spread between 20 and 14 Ma, while biotite Rb-Sr dating yielded ages of 15.5 to 13.1 Ma [*Dempster*, 1986] (Figure 9). Later, in combination with structural mapping, biotite and white mica ^{39}Ar/^{40}Ar ages in stage 1 shear zones have generally been interpreted to date crystallization rather than cooling. *Challandes et al*. [2008] and *Rolland et al*. [2009] were able to measure biotite in stage 1 shear zones yielding Ar-Ar ages of 21.2 ± 0.7 to 17.2 ± 0.6 Ma, with white micas giving an age range of 19.4 ± 0.6 to 16.7 ± 0.7 Ma. Little deformed country rock gave partly reset Rb-Sr pseudo isochrons of 25.1 ± 0.7 to 15.9 ± 0.4 Ma [*Challandes et al*., 2008]. These oldest ages are in line with regional considerations of thrusting in the Aar Massif and related deformation in the Helvetic Alps [*Pfiffner*, 2009].

White mica ages of stage 2 are 13.8 ± 0.1 to 12.2 ± 0.2 Ma [*Rolland et al*., 2009]. The youngest of these ages overlap with Rb-Sr whole-rock-mica ages from mylonites of 12.2 ± 1.3 to 10 ± 0.3 Ma [*Challandes et al*., 2008].

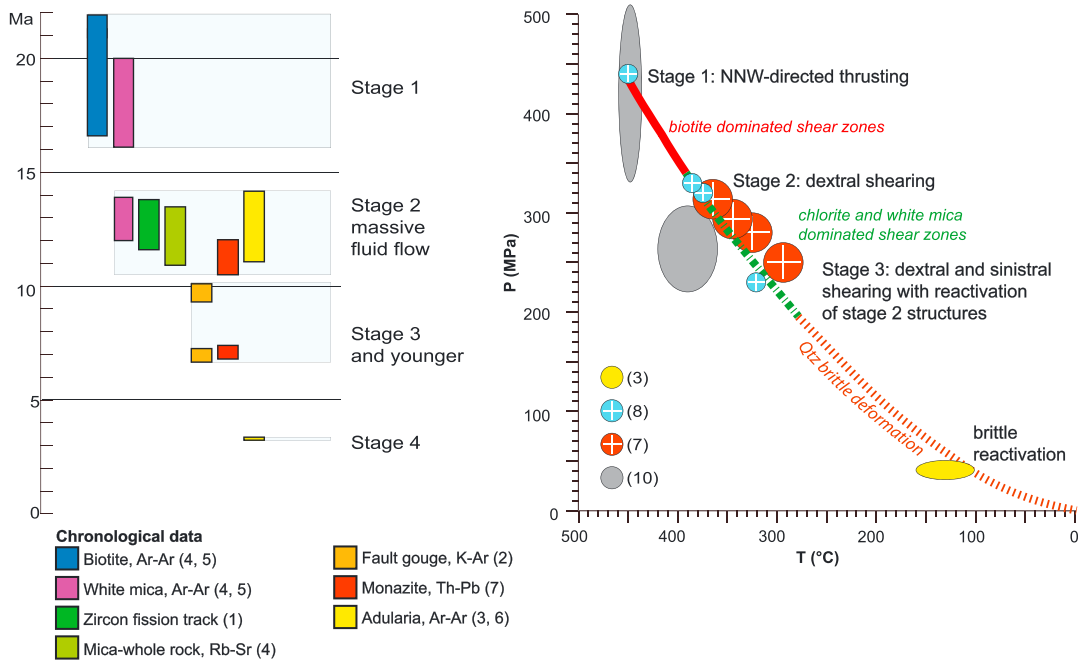

Figure 9. Selected trace element diagrams. The colored ellipses mark the youngest/outer zones in each grain, with the dashed ellipsis marking a zone giving mixed ages and showing signs of recrystallization.

Zircon fission track ages (ZFT) in the Grimsel area are 13.1 ± 0.7 to 12.4 ± 0.6 Ma [*Michalski and Soom*, 1990].

We interpret the monazite ages as crystallization related to massive fluid flow during the formation of stage 2 shear zones, also affecting the older horizontal cleft generation (PK2 sample) close to the shear zone. These coeval ages of different minerals and isotopic systems (Ar-Ar muscovite, whole-rock-mica Rb-Sr in mylonites, and ZFT) suggest a time of strong fluid-rock interaction causing new crystallization of minerals [e.g., *Villa and Hanchar*, 2013; *Diamond and Tarantola*, 2015], making it possible to link monazite crystallization with the quartz fluid inclusion record [*Mullis*, 1996; this study]. Monazite and adularia from horizontal clefts elsewhere in the Aar Massif yielded older ages of 14.51 ± 0.26, 14.01 ± 0.09, and 13.72 ± 0.11 Ma [*Janots et al.*, 2012; *Rauchenstein-Martinek*, 2015]. This shows that the end of thrusting and the final switch to dextral shearing occurred in the Grimsel area in the time around 12–11 Ma.

The related change in σ_2 and σ_3 (Figure 2b) was not abrupt, but gradual or stepwise, indicated by the occurrence of intermediate stages as seen in oblique, ~45° dipping, stretching lineations (Figure 2c) and associated rare cleft planes. At a larger scale, this event coincides with a continued underthrusting of the European crust during formation of the Jura belt at 12–10 Ma and coeval strike-slip deformational tectonic activity of the Rhone-Simplon line at the time of 14–11 Ma [*Campani et al.*, 2010].

After ~11 Ma, deformation continued in a strike-slip environment and led to the reactivation of some of the stage 2 shear zones. Fault gouge and mylonitic material of the Grimsel region yielded a range of K-Ar ages of ~10.5 down to ~7 Ma [*Kralik et al.*, 1992]. This directly postdates cleft monazite formation in the Grimsel area and fault gouge K-Ar ages from two similarly N-Ne trending shear zones to the SW of the Grimsel shear zone, 13.6 ± 0.3 to 10.3 ± 0.6 Ma. This is in line with *Pleuger et al.* [2012], who observed a south to north younging of fault gouge ages in the Central Alps.

Later partial recrystallization of monazite in Grim 3 at 7.02 ± 0.31 Ma coincides with the youngest fault gouge ages of ~7 Ma in the Grimsel area [*Kralik et al.*, 1992]. This younger age also compares well to ^{232}Th-^{208}Pb cleft monazite crystallization ages in structurally similar clefts of 8.03 ± 0.22 to 6.25 ± 0.60 Ma from the Baltschieder Valley, southwestern Aar Massif [*Berger et al.*, 2013] (Figure 1) and 7.2 ± 0.4 to 5.4 ± 0.5 Ma in the Belledonne Massif [*Gasquet et al.*, 2010]. This deformation episode in the Grimsel area can thus be kinematically linked to tectonic activity along the Rhone-Simplon Faults [e.g., *Campani et al.*, 2010, 2014] and probably coeval dextral

strike-slip faulting in the Belledonne Massif [*Hubbard and Mancktelow*, 1992] and Ornon-Roselend fault [*Gasquet et al*., 2010]. This deformation episode postdates the ductile deformation along the Simplon Fault Zone continuing until around 14 to 11 Ma (^{40}Ar-^{39}Ar on white mica close to the southern Aar Massif [*Campani et al*., 2010]). This is consistent with the youngest cooling history (Figure 9) and the three secondary fluid inclusion populations documented in quartz crystals from the vertical GRIM4 cleft (Table 2). The youngest age of 3.30 ± 0.06 Ma is recorded by adularia formed at 100–160°C in stage 2 parallel brecciated zones [*Hofmann et al*., 2004] and is assigned here to represent stage 4, the latest hydrothermal activity recorded by datable mineral growth.

7. Conclusions

The dating of hydrothermal cleft monazite crystallization around ~12–11 Ma, at ~370°C and 320–330 MPa, fills the gap between white mica Ar-Ar ages and fault gouge K-Ar ages for the Grimsel area. The occurrence of these ages in both older horizontal and younger vertical clefts shows, when coupled with structural data, that the end of the gradual transition from thrusting to dextral shearing likely occurred around this time. An additional monazite age of 7.02 ± 0.31 Ma in the younger vertical clefts confirms the validity of the youngest fault ages for the area. This younger deformation can be associated to activity along the Rhone-Simplon Faults and possibly down into the Belledonne Massif. These ages, along with fluid inclusion data indicating repeated shear zone reactivation, allow a more detailed reconstruction of the area's tectonic evolution.

Our data show that cleft monazite is a good method for dating shear zone activity. Older ages always represent initial crystallization, unique among current methods of dating lower-greenschist facies deformation. This can be supplemented by partial dissolution-reprecipitation/recrystallization ages, as monazite has the potential to remain reactive within a cleft over times of several million years.

Acknowledgments

The data used are listed in references, tables, and supporting information. The NordSim ion microprobe is operated by the research funding agencies of Denmark, Iceland, Norway, and Sweden; the Geological Survey of Finland; and the Swedish Museum of Natural History. This study was financed by the Swiss National Foundation grant 200021-143972. Jean-Marie Boccard is thanked for help with sample preparation. Agathe Martignier and André Piuz are thanked for help with the scanning electron microscope and Lukas Aschwanden for help with the Spindel Stage. Lev Ilyinsky and Kerstin Lindén are thanked for the help during measurements at the NordSim facility and Gemma de la Flor Martin for the help with figure preparation. We would like to thank Claudio Faccenna for his patient editing work, as well as Elizabeth Catlos and Neil Mancktelow for their detailed reviews, which considerably improved the manuscript.

References

Aleinikoff, J. N., W. S. Schenck, M. O. Plank, L. Srogi, C. M. Fanning, L. Kamo, and H. Bosbyshell (2006), Deciphering igneous and metamorphic events in high-grade rocks of the Wilmingtion Complex, Delaware: Morphology, cathodoluminescence and backscattered electron zoning, and SHRIMP U-Pb geochronology of zircon and monazite, *Geol. Soc. Am. Bull.*, *118*, 39–64, doi:10.1130/B25659.1.

Bakker, R. J. (1999), Adaptation of the Bowers and Helgeson (1983) equation of state to the H_2O-CO_2-CH_4-N_2-NaCl system, *Chem. Geol.*, *154*, 225–236, doi:10.1016/S0009-2541(98)00133-8.

Bakker, R. J., and L. W. Diamond (2006), Estimation of volume fractions of liquid and vapor phases in fluid inclusions, and definition of inclusion shapes, *Am. Mineral.*, *91*, 635–657, doi:10.2138/am.2006.1845.

Berger, A., E. Gnos, E. Janots, M. Whitehouse, M. Soom, R. Frei, and T. E. Waight (2013), Dating brittle tectonic movements with cleft monazite: Fluid-rock interaction and formation of REE minerals, *Tectonics*, *32*, 1–14, doi:10.1002/tect.20071.

Bodnar, R. J. (1993), Revised equation and table for determining the freezing point depression of H_2O-NaCl solutions, *Geochim. Cosmochim. Acta*, *57*, 683–684, doi:10.1016/0016-7037(93)90378-A.

Bodnar, R. J., and M. O. Vityk (1994), Interpretation of microthermometric data for H_2O-NaCl fluid inclusions, in *Fluid Inclusions in Minerals: Methods and Applications*, edited by B. de Vivo and M. L. Frezzotti, pp. 117–130, Short Course IMA, VPI Press, Blacksburg, Va.

Bowers, T. S., and H. C. Helgeson (1983), Calculation of the thermodynamic and geochemical consequences of non ideal mixing in the system H_2O-CO_2-NaCl on phase relations in geologic systems. Equation of state for H_2O-CO_2-NaCl fluids at high pressures and temperatures, *Geochim. Cosmochim. Acta*, *47*, 1247–1275, doi:10.1016/0016-7037(83)90066-2.

Bozzo, A. T., H.-S. Chen, J. R. Kass, and A. J. Barduhn (1973), The properties of the hydrates of chlorine and carbon dioxide, in *The Fourth International Symposium on Fresh Water from the Sea*, vol. 3, edited by A. Delyannis and E. Delyannis, pp. 437–451, Elsevier Sci. Comp., Amsterdam.

Campani, M., N. Mancktelow, D. Seward, Y. Rolland, W. Müller, and I. Guerra (2010), Geochronological evidence for continuous exhumation through the ductile-brittle transition along a crustal scale low-angle normal fault: Simplon Fault Zone, Central Alps, *Tectonics*, *29*, TC3002, doi:10.1029/2009TC002582.

Campani, M., N. Mancktelow, and G. Courrioux (2014), The 3D interplay between folding and faulting in a syn-orogenic extensional system: The Simplon Fault Zone in the Central Alps (Switzerland and Italy), *Swiss J. Geosci.*, *107*, 251–271, doi:10.1007/s00015-014-0163-y.

Catlos, E. J. (2013), Generalizations about monazite: Implications for geochronologic studies, *Am. Mineral.*, *98*, 819–832, doi:10.2138/am.2013.4336.

Challandes, N., D. Marquer, and I. M. Villa (2008), P-T-t modelling, fluid circulation, and ^{39}Ar-^{40}Ar and Rb-Sr mica ages in the Aar Massif shear zones (Swiss Alps), *Swiss J. Geosci.*, *101*, 269–288, doi:10.1007/s00015-008-1260-6.

Cherniak, D. J., and J. M. Pyle (2008), Th diffusion in monazite, *Chem. Geol.*, *256*, 52–61, doi:10.1016/j.chemgeo.2008.07.024.

Corfu, F. (1988), Differential response of U-Pb systems in coexisting accessory minerals, Winnipeg River Subprovince, Canadian Shield: Implications for Archean crustal growth and stabilization, *Contrib. Min. Petrol.*, *98*, 312–325, doi:10.1007/BF00375182.

Dempster, T. (1986), Isotope systematics in minerals biotite rejuvenation and exchange during Alpine metamorphism, *Earth Planet. Sci. Lett.*, *67*, 355–367, doi:10.1016/0012-821X(86)90003-8.

Diamond, L. W., and A. Tarantola (2015), Interpretation of fluid inclusions in quartz defomed by weak ductile shearing: Reconstruction of differential stress magnitudes and pre-deformation fluid properties, *Earth Planet. Sci. Lett.*, *417*, 107–119, doi:10.1016/j.epsl.2015.02.019.

Dollinger, H. (1989), Petrographische und geochemische Untersuchungen des Altkristallins zwischen Nägelisgrätli und Oberaarjoch (Grimsel, Kt Bern) und hydrothermale Veränderungen granitischer Gesteine in der Grimselregion (mittleres Aarmassiv), diploma thesis, Univ. Bern, Switzerland.

Drummond, S. E. (1981), Boiling and mixing of hydrothermal fluids: Chemical effects on mineral precipitation, PhD thesis, Pennsilvania State Univ., Pa.

Gardés, E., O. Jaoul, J.-M. Montel, A.-M. Seydoux-Guillaume, and R. Wirth (2006), Pb diffusion in monazite: An experimental study of $Pb^{2+} + Th^{4+} \leftrightarrow 2Nd^{3+}$ interdiffusion, *Geochim. Cosmochim. Acta*, *70*, 2325–2336, doi:10.1016/j.gca.2006.01.018.

Gasquet, D., J.-M. Bertrand, J.-L. Paquette, J. Lehmann, G. Ratzov, R. De Ascencao Guedes, M. Tiepolo, A.-M. Boullier, S. Scaillet, and S. Nomade (2010), Miocene to Messinian deformation and hydrothermal activity in a pre-Alpine basement massif of the French western Alps: New U-Th-Pb and Argon ages from the Lauzière Massif, *Bull. Soc. Géol. Fr.*, *181*, 227–241, doi:10.2113/gssgfbull.181.3.227.

Giudotti, C. V. (1984), Micas in metamorphic rocks, in *Micas*, edited by S. W. Bailey, pp. 357–467, Mineral. Soc. of America, Chantilly, Va.

Gnos, E., E. Janots, A. Berger, M. Whitehouse, F. Walter, T. Pettke, and C. Bergemann (2015), Age of cleft monazites in the eastern Tauern Window: Constraints on crystallization conditions of hydrothermal monazite, *Swiss J. Geosci.*, *108*, 55–74, doi:10.1007/s00015-015-0178-z.

Goncalves, P., E. Oliot, D. Marquer, and J. A. D. Conolly (2012), Role of chemical processes on shear zone formation: An example from the Grimsel metagranodiorite (Aar Massif, Central Alps), *J. Metamorph. Geol.*, *30*, 703–722, doi:10.1111/j.1525-1314.2012.00991.x.

Gray, A. L. (1985), Solid sample introduction by laser ablation for inductively coupled plasma source-mass spectrometry, *Analyst*, *110*, 551–556, doi:10.1039/AN9851000551.

Guillong, M., D. L. Meier, M. M. Allan, C. A. Heinrich, and B. W. D. Yardley (2008), Appendix A6: SILLS: A matlab-based program for the reduction of laser ablation ICP-MS data of homogeneous materials and inclusions, in *Mineralogical Association of Canada Short Course*, vol. 40, edited by P. Sylvester, pp. 328–333, Mineral. Assoc. of Canada, Vancouver, B. C.

Harrison, T. M., K. D. McKeegan, and P. LeFort (1995), Detection of inherited monazite in the Manaslu leucogranite by ion microprobe dating: Crystallization age and tectonic implications, *Earth Planet. Sci. Lett.*, *133*, 271–282, doi:10.1016/0012-821X(95)00091-P.

Heijboer, T. C. (2006), Origin and pathways of pro- and retrograde fluids, PTt paths and fluid-mineral equilibria from Alpine veins of the Central Alps: Case studies of the Fibbia and Amsteg areas, PhD thesis, Univ. of Basel, Basel, Switzerland.

Hofmann, B. A., M. Helfer, L. W. Diamond, I. M. Villa, R. Frei, and J. Eikenberg (2004), Topography-driven hydrothermal breccia mineralization of Pliocene age at Grimsel Pass, Aar massif, Central Swiss Alps, *Schweiz. Mineral. Petrogr. Mitt.*, *84*, 271–302, doi:10.5169/seals-63750.

Hubbard, M., and N. S. Mancktelow (1992), Lateral displacement during Neogene convergence in the western and Central Alps, *Geology*, *20*, 943–946, doi:10.1130/0091-7613(1992).

Jäger, E., E. Niggli, and A. E. Wenk (1967), Rb-Sr-Altersbestimmungen an Glimmern der Zentralalpen, Beitr. Geol. Karte Schweiz, N.F. 134, 1-76.

Janots, E., A. Berger, E. Gnos, M. Whitehouse, E. Lewin, and T. Pettke (2012), Constraints on fluid evolution during metamorphism from U-Th-Pb systematics in Alpine hydrothermal monazite, *Chem. Geol.*, *326-327*, 61–71, doi:10.1016/j.chemgeo.2012.07.014.

Kirkland, C. L., M. J. Whitehouse, and T. Slagstad (2009), Fluid-assisted zircon and monazite growth within shear zones: A case study from Finnmark, Arctic Norway, *Contrib. Mineral. Petrol.*, *158*, 637–657, doi:10.1007/s00410-009-0401-x.

Kralik, M., N. Clauer, R. Holnsteiner, H. Huemer, and F. Kappel (1992), Recurrent fault activity in the Grimsel Test Site (GTS, Switzerland): Revealed by Rb-Sr, K-Ar and tritium isotope techniques, *J. Geol. Soc.*, *149*, 293–301, doi:10.1144/gsjgs.149.2.0293.

Ludwig, K. (2009), *Isoplot v.3.71: A Geochronological Toolkit for Microsoft Excel*, *Spec. Publ.*, vol. 4, 70 pp., Berkeley Geochronology Center, Berkeley, Calif.

Marquer, D. (1989), Transferts de matieres et déformation des granitoides. Aspects méthodologiques, *Schweiz. Mineral. Petrogr. Mitt.*, *69*, 13–33.

Marquer, D., D. Gapais, and R. Capdevila (1985), Comportement chimique et orthogneissification d'une granodiorite en faciès schistes verts (Massif de l'Aar, Alpes centrales suisses), *Bull. Mineral.*, *108*, 209–221.

Massone, H. J., and W. Schreyer (1987), Phengite geobarometry based on the limiting assemblage with K-feldspar, phlogopite and quartz, *Conrib. Mineral. Petrol.*, *96*, 212–224, doi:10.1007/BF00375235.

Massone, H. J., and W. Schreyer (1989), Stability field of the high-presure assemblage talc + phengite and two new phengite barometers, *Eur. J. Mineral.*, *1*, 391–410, doi:10.1127/ejm/1/3/0391.

Megger, W. F., and F. O. Westfall (1950), Lamps and wavelengths of mercury 198, *J. Res. Natl. Bur. Stand.*, *44*, 447–455.

Meldrum, A., L. A. Boatner, W. J. Weber, and R. C. Ewing (1998), Radiation damage in zircon and monazite, *Geochim. Cosmochim. Acta*, *62*, 2509–2520, doi:10.1016/S0016-7037(98)00174-4.

Meldrum, A., L. A. Boatner, S. J. Wang, S. X. Wang, and R. C. Ewing (1999), Effects of dose rate and temperature on the crystalline-to-metamict transformation in the ABO(4) orthosilicates, *Can. Mineral.*, *37*, 207–221.

Meldrum, A., L. A. Boatner, and R. C. Ewing (2000), A comparison of radiation effects in crystalline ABO(4)-type phosphates and silicates, *Min. Mag.*, *64*, 185–194.

Mercolli, I., F. Schenker, and H. A. Stalder (1984), Geochemische Veränderungen von Granit durch hydrothermale Lösungen (Zentraler-Aaregranit, Gotthard-Strassentunnel), *Schweiz. Mineral. Petrogr. Mitt.*, *64*, 67–82.

Michalski, I., and M. Soom (1990), The Alpine thermo-tectonic evolution of the Aar and Gotthard Massifs, Central Switzerland: Fission track ages on zircon and apatite and K-Ar mica ages, *Schweiz. Mineral. Petrogr. Mitt.*, *70*, 373–387.

Mullis, J. (1976), Die Quarzkristalle des Val d'Illiez - Zeugen spätalpiner Bewegungen, *Eclogae Geol. Helv.*, *69*, 343–357.

Mullis, J. (1995), Genesis of Alpine fissure minerals, Leica, Scientific and Technical Information XI, 2, 54-64.

Mullis, J. (1996), P-T-t path of quartz formation in extensional veins of the Central Alps, *Schweiz. Mineral. Petrogr. Mitt.*, *76*, 159–164.

Mullis, J., J. Dubessy, B. Poty, and J. O'Neil (1994), Fluid regimes during late stages of a continental collision: Physical, chemical, and stable isotope measurements of fluid inclusions in fissure quartz from a geotraverse through the Central Alps, Switzerland, *Geochim. Cosmochim. Acta*, *58*, 2239–2267, doi:10.1016/0016-7037(94)90008-6.

Nasdala, L., F. Finger, and P. Kinny (1999), Can monazite become metamict?, *Eur. J. Mineral.*, *11*, 164.

Oberhänsli, R., F. Schenker, and I. Mercolli (1988), Indications of Variscan nappe tectonics in the Aar Massif, *Schweiz. Mineral. Petrogr. Mitt.*, *68*, 509–520.

Parker, R. L. (1954), *Die Mineralienfunde der Schweizer Alpen*, 311 pp., Wepf & Co, Basel.

Pettke, T., F. Oberli, A. Audetat, M. Guillong, A. C. Simon, J. J. Hanley, and L. M. Klemm (2012), Recent developments in element concentration and isotope ratio analysis of individual fluid inclusions by laser ablation single and multiple collector ICP-MS, *Ore Geol. Rev.*, *44*, 10–38, doi:10.1016/j.oregeorev.2011.11.001.

Pleuger, J., N. Mancktelow, H. Zwingmann, and M. Manser (2012), K-Ar dating of synkinematic clay gouges from Neoalpine faults of the Central, Western and Eastern Alps, *Tectonophysics*, *550-553*, 1–16, doi:10.10116/j.tecto.2012.05.001.

Pfiffner, O. A. (2009), *Geologie der Alpen*, UTB, Stuttgart, Germany.

Potter, R. W., M. A. Clynne, and D. L. Brown (1978), Freezing point depression of aqueous sodium solutions, *Econ. Geol.*, *73*, 284–285, doi:10.2113/gsecongeo.73.2.284.

Poty, B. (1969), La croissance des cristaux de quartz dans les filons sur l'exemple du filon de la Gardette (Bourg d'Oisans) et des filons du massif du Mont Blanc, thèse Univ. de Nancy Sciences de la Terre, Mém. 17. Nancy.

Poty, B. P., H.-A. Stalder, and A. M. Weisbrod (1974), Fluid inclusion studies in quartz from fissures of western and Central Alps, *Schweiz. Mineral. Petrogr. Mitt.*, *54*, 717–752.
Putnis, A. (2002), Mineral replacement reactions: From macroscopic observations to microscopic mechanisms, *Min. Mag.*, *66*, 689–708.
Putnis, A. (2009), Mineral replacement reactions, *Rev. Mineral. Geochem.*, *70*, 87–124.
Rauchenstein-Martinek, K. (2015), Metamorphic fluid history along a cross section through the Central Alps: Constraints from LA-ICPMS analysis of fluid inclusions and Ar-Ar geochronology, PhD thesis, 89 pp., ETH Zürich, Zürich, Switzerland.
Rolland, Y., S. F. Cox, and M. Corsini (2009), Constraining deformation stages in brittle-ductile shear zones from combined field mapping and 40Ar/39Ar dating: The structural evolution of the Grimsel Pass area (Aar Massif, Swiss Alps), *J. Struct. Geol.*, *31*, 1377–1394, doi:10.1016/j.jsg.2009.08.003.
Rossi, M., and Y. Rolland (2014), Stable isotope and Ar/Ar evidence of prolonged multi-scale fluid flow during exhumation of orogenic crust: Example from the Mont Blanc and Aar Massifs (NW Alps), *Tectonics*, *33*, 1681–1709, doi:10.1002/2013TC003438.
Schmid, S., B. Fügenschuh, E. Kissling, and R. Schuster (2004), The tectonic map and overall structure of the Alpine orogeny, *Eclogae Geol. Helv.*, *97*, 93–117, doi:10.1007/s00015-004-1113-x.
Seydoux-Guillaume, A.-M., J.-L. Paquette, M. Wiedenbeck, J.-M. Montel, and W. Heinrich (2002), Experimental resetting of the U-Th-Pb systems in monazite, *Chem. Geol.*, *191*, 165–181, doi:10.1016/S0009-2541(02)00155-9.
Sharp, Z. D., H. Masson, and R. Lucchini (2005), Stable isotope geochemistry and formation mechanisms of quartzt veins; extreme paleoaltitudes of the Central Alps in the Neogene, *Am. J. Sci.*, *305*, 187–219, doi:10.2475/ajs.305.3.187.
Stacey, J., and J. Kramers (1975), Approximation of terrestrial lead isotope evolution by a two-stage model, *Earth Planet. Sci. Lett.*, *26*, 207–221, doi:10.1016/0012-821X(75)90088-6.
Stalder, H.-A. (1964), Petrographische und mineralogische Untersuchungen im Grimselgebiet BE, *Schweiz. Mineral. Petrogr. Mitt.*, *44*, 188–398.
Steck, A. (1968), Die alpidischen Strukturen in den Zentralen Aaregraniten des westlichen Aarmassivs, *Eclogae Geol. Helv.*, *61*, 19–48, doi:10.5169/seals-163584.
Steiger, R. H., and E. Jäger (1977), Convention of the use of decay constants in geo- and cosmochronology, *Earth Planet. Sci. Lett.*, *36*, 359–362, doi:10.1016/0012-821X(77)90060-7.
Villa, I. M., and J. M. Hanchar (2013), K-feldspar hygrochronology, *Geochim. Cosmochim. Acta*, *101*, 24–33.
Wehrens, P. (2015). Structural evolution in the Aar Massif (Haslital transect): Implications for mid-crustal deformation, PhD thesis, 151 pp., Univ. of Bern, Switzerland, doi:10.1016/j.gca.2012.09.047.
Zhang, Y. G., and J. D. Frantz (1987), Determination of the homogenization temperatures and densities of supercritical fluids in the system NaCl-KCl-$CaCl_2$-H_2O using synthetic fluid inclusions, *Chem. Geol.*, *64*, 335–350, doi:10.1016/0009-2541(87)90012-X.